

# DEEP DECOMPOSITION METHOD FOR THE LIMITED APERTURE INVERSE OBSTACLE SCATTERING PROBLEM

YUNWEN YIN\* AND LIANG YAN †

**Abstract.** In this paper, we consider a deep learning approach to the limited aperture inverse obstacle scattering problem. It is well known that traditional deep learning relies solely on data, which may limit its performance for the inverse problem when only indirect observation data and a physical model are available. A fundamental question arises in light of these limitations: is it possible to enable deep learning to work on inverse problems without labeled data and to be aware of what it is learning? This work proposes a deep decomposition method (DDM) for such purposes, which does not require ground truth labels. It accomplishes this by providing physical operators associated with the scattering model to the neural network architecture. Additionally, a deep learning based data completion scheme is implemented in DDM to prevent distorting the solution of the inverse problem for limited aperture data. Furthermore, apart from addressing the ill-posedness imposed by the inverse problem itself, DDM is a physics-aware machine learning technique that can have interpretability property. The convergence result of DDM is theoretically proven. Numerical experiments are presented to demonstrate the validity of the proposed DDM even when the incident and observation apertures are extremely limited.

**Keywords:** inverse scattering problem; limited aperture; deep learning; deep decomposition method.

**1. Introduction.** Inverse scattering problems are common in many industrial and engineering applications, such as nondestructive testing [1], radar imaging [8] and medical imaging [27]. The majority of inverse scattering problems are non-linear and specifically ill-posed, meaning that the solution may not exist or may not be unique, and, more importantly, it fails to depend continuously on the data, causing a minor perturbation in the data to cause a massive deviation in the solution. As a result, achieving stable and accurate numerical solutions is extremely difficult. There are numerous numerical methods using full aperture data for such inverse problems, such as the Newton-type iterative method [26, 17], the optimization method [24], the recursive linearization method [4, 6], the linear sampling method [9, 13], the direct sampling method [19, 29] and the factorization method [25, 43]. However, the incident and observation apertures are typically restricted due to the limitations of practical settings; consequently, inverse scattering problems with limited aperture data result in increased non-linearity and ill-posedness. Several reconstruction techniques have been proposed [3, 5, 18, 21], by directly utilizing limited aperture measurements. Unfortunately, no classical numerical method can maintain the high-quality inversions for limited aperture problems, not even quantitative optimization or iterative methods. Reconstruction techniques using the recovered full aperture data are a natural remedy that involves first recovering data for all incident and observation angles [14, 32, 16]. Because the inversion process is split into two parts, this approach also increases the computational cost even though the inversion quality is improved. Furthermore, the inverse problems in traditional approaches must inevitably be solved again when new observation data are used, which restricts the potential for real-time reconstructions, particularly for iterative algorithms.

Recently, deep neural networks(DNNs) have demonstrated their promising features in a variety of inverse problems [28, 15, 48, 44, 37, 30, 39, 38]. In contrast to classical physics-based inversion methods, DNNs typically do not rely on the underlying physics, but the trade-off is that they are restricted to be purely data-driven and rooted in the big data regime. As a result, they will always be unable to solve the inverse problem: one can not obtain the quantity of interest known as labeled data, but only indirect observation data and a physical model. To address these issues, one natural solution is to provide DNNs with the governing physics. In [41], physics-informed neural networks (PINNs) were proposed for solving the forward and inverse problems by constraining physical knowledge of governing equations into the loss function. However, in the original forms of PINNs, unknown parameters in inverse problems are only taken into account as constants, and they are updated together with weights and biases of neural networks. In order to develop PINNs for the

\*School of Mathematics, Southeast University, Nanjing, China.

†School of Mathematics, Southeast University, Nanjing, China. Email:yanliang@seu.edu.cn. LY's work was supported by the NSF of China (Nos. 92370126, 12171085).

scenario where the unknown parameters are functions, two networks must be trained concurrently: one for the partial differential equation solutions and another for the unknown parameters; see [33, 42, 45, 47] and the references therein. We also strongly refer the readers to [7] for other relevant work called weak adversarial network[46] that possesses the similar methodology for inverse problems. Although PINNs have shown great potential in solving various inverse problems, similar to classical methods, they have to be learned again for given new observation data.

We argue that learning the inverse operator directly is the more effective way to effectively avoid the retraining issues. In this scenario, real-time reconstructions can be achieved by the neural network once it has been trained. However, due to the ill-posedness of the inverse problems, the inverse operator is often an unbounded operator and always lacks the existence and uniqueness, making this an extremely difficult task. This also explains why the current little effort is focused only on learning the inverse operator through data-driven methods. The works [40, 36] focused on constraining forward mappings into their loss functions in order to take advantage of physics information. They proposed physics-aware neural networks and model-constrained Tikhonov networks, respectively. The works [22, 35], in contrast to [40, 36], concentrated on carefully planning the hidden layer structures in neural networks by utilizing the properties of the analyzed inverse problems. These works provide two effective methods to leverage physics information; on the other hand, there are still many inverse problems for which an alternative approach must be found due to the high difficulty of embedding the forward operators into the loss functions or indirectly introducing physics information into the hidden layers.

Inspired by the aforementioned discussions, we present in this work a physics-aware deep decomposition approach for the limited aperture inverse obstacle scattering problem. Due to the unbounded nature of the inverse operator associated with acoustic obstacle scattering and the high ill-posedness caused by the limited aperture, learning the inverse operator will be extremely challenging. As a result, regularization techniques must be used in the network structure or optimization process. This is accomplished by constraining a penalty term created by the Herglotz operator into the deep decomposition method (DDM) loss function. Moreover, we use the scattering information, which includes the Herglotz operator, the far-field operator, and the fundamental solution, in place of the forward mapping to construct the loss function. In fact, it is numerically intractable to directly embed the forward mapping of the acoustic obstacle scattering problem into the network because the forward solver, which is typically based on the boundary integral equation method or the finite element method, is quite complicated. On the other hand, DDM takes into consideration a deep learning-based data retrieval strategy that incorporates a convolution neural network, which is motivated by the research presented in [16]. To the best of our knowledge, the proposed DDM is the first work both retrieving full aperture data and exploiting the physical information associated with the acoustic obstacle scattering model in the neural network for the impenetrable obstacle detection. In DDM, the parameters of neural network are updated simultaneously, allowing for the reconstruction of both the boundary and the entire aperture data at the same time, unlike the works [14, 32, 16] where the inversion process is split into two parts. We summarize the main features and novelties of our proposed DDM as follows:

- DDM is the first physics-aware machine learning approach to tackle the limited aperture inverse obstacle scattering problem. It combines deep learning, physical information, data retrieval, and boundary recovery techniques. More importantly, DDM is more aware of what it is learning and has some interpretability thanks to the physical information.
- DDM does not require exact boundary information, also referred to as labeled data, during the training phase. DDM can resolve the ill-posedness caused by the relevant inverse problem by adding a regularization term associated to the Herglotz operator into the loss function. Because DDM is trained with the guidance of the underlying physics information, it can learn the regularized inverse operator more efficiently.
- Theoretically, we rigorously prove DDM’s convergence result using the properties of the

far-field and Herglotz operators. We also demonstrate that adding relatively small noise to measured limited aperture data is useful for investigating additional properties of the inverse operator.

- We demonstrate the effectiveness of our proposed DDM using numerical examples. It clearly shows that DDM can produce satisfactory reconstructions even when the incident and observation apertures are both extremely limited. Moreover, DDM has the benefit of real-time numerical computation because, once trained, it can solve the inverse problem in terms of forward propagation.

The rest of the paper is organized as follows. In the following section, we present the basis setup and preliminary results for the acoustic inverse obstacle scattering model. In Section 3, we present the DDM with its convergence result and discretization form. Numerical experiments are given in Section 4 to show the promising features of DDM and conclusions are finally made in Section 5.

**2. Problem setup and preliminaries.** Assume that  $D \subset \mathbb{R}^2$  is an open and bounded simply connected domain with a  $C^2$ -boundary  $\partial D$ . The incident field  $u^i$  is given by

$$u^i(x) := u^i(x, d) = e^{ikx \cdot d}, \quad x \in \mathbb{R}^2, \quad (2.1)$$

where  $i := \sqrt{-1}$  is the imaginary unit,  $k \in \mathbb{R}_+$  is the wavenumber and  $d \in S := \{x \in \mathbb{R}^2 : |x| = 1\}$  is the direction of the propagation. The presence of the impenetrable obstacle  $D$  interrupts the propagation of the incident wave  $u^i$ , yielding the exterior scattered field  $u^s$ . The direct scattering problem for the sound-soft obstacle is to find  $u^s = u - u^i$  satisfying the Helmholtz equation

$$\Delta u^s + k^2 u^s = 0, \quad \text{in } \mathbb{R}^2 \setminus \overline{D}, \quad (2.2)$$

with the Dirichlet boundary condition

$$u^s + u^i = 0, \quad \text{on } \partial D, \quad (2.3)$$

where  $u$  is the total field. In addition, the following Sommerfeld radiation condition

$$\lim_{r \rightarrow \infty} r^{\frac{1}{2}} \left( \frac{\partial u^s}{\partial r} - ik u^s \right) = 0, \quad r = |x|, \quad (2.4)$$

holds, which characterizes the outgoing nature of the scattered field  $u^s$ . It is well known that the forward scattering problem (2.2)-(2.4) is well-posed (cf. [10, 34]). The scattered field  $u^s$  also has the asymptotic behavior

$$u^s(x) = \frac{e^{ikr}}{\sqrt{r}} \left\{ u^\infty(\hat{x}) + \mathcal{O}\left(\frac{1}{r}\right) \right\}, \quad r = |x| \rightarrow \infty, \quad (2.5)$$

uniformly in all directions  $\hat{x} = x/|x| \in S$ . Here,  $u^\infty(\hat{x})$ , which is called the far-field pattern of the scattered field, is an analytic function on  $S$ . In what follows, we write  $u^\infty(\hat{x}, d)$  to signify such far-field data and specify its dependence on the observation direction  $\hat{x}$  and the incident direction  $d$ .

The inverse scattering problem we are concerned with is to recover the boundary  $\partial D$  from the limited aperture data  $u^\infty(\hat{x}, d)$  for  $(\hat{x}, d) \in \gamma^o \times \gamma^i$  at a fixed wavenumber  $k$ , where  $\gamma^o \subset S$  and  $\gamma^i \subseteq S$  are respectively the limited observation and incident aperture. Fig. 2.1 shows an illustration of the inverse problem. Define a non-linear forward operator  $\mathcal{G}$  that maps the boundary to the corresponding far-field pattern, the above mentioned inverse problem can be formulated as follows:

$$\partial D = \mathcal{G}^{-1}(u^\infty(\hat{x}, d)), \quad (\hat{x}, d) \in \gamma^o \times \gamma^i. \quad (2.6)$$

In this work, we aim to apply a physics-aware machine learning approach to solve the inverse problem (2.6). In contrast to traditional purely data-based neural networks, we focus on providing

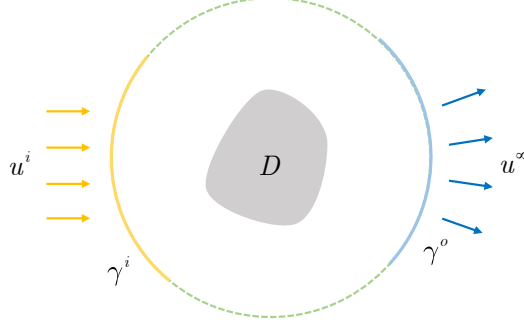


FIG. 2.1. A schematic illustration of the limited aperture inverse obstacle scattering problem.

a specially constructed neural network in conjunction with the physics information. To this end, the remainder of this section summarizes the preliminary results for the acoustic inverse obstacle scattering model using the full aperture data. We first define a superposition of the incident plane waves by

$$v^i(x) = \int_S e^{ikx \cdot d} g(d) ds(d), \quad x \in \mathbb{R}^2, \quad (2.7)$$

with the weight function  $g$ . In this case,  $v^i$  is also referred to a Herglotz wave function, where  $g$  is the Herglotz kernel.

Let us define the following interior boundary value problem, assuming that  $k^2$  is not a Dirichlet eigenvalue to the negative Laplacian in  $D$ :

$$\begin{cases} \Delta v^i(x) + k^2 v^i(x) = 0, & \text{in } D, \\ v^i(x) = -\Phi(x, z), & \text{on } \partial D, \end{cases} \quad (2.8)$$

where  $\Phi(x, z) = \frac{i}{4} H_0^{(1)}(k|x-z|)$  is the outgoing Green function of Helmholtz equation in  $\mathbb{R}^2$  and  $H_0^{(1)}$  is the Hankel function of the first kind of order zero. Moreover, the point  $z$  is contained in the sound-soft obstacle  $D$ . Then, we can connect this boundary value problem (2.8) to the scattering problem (2.2)-(2.4). Taking  $v^i$  in (2.7) as the incident wave to (2.2)-(2.4), one can have the corresponding far-field pattern that is associated with the far-field operator  $F : L^2(S) \rightarrow L^2(S)$

$$(Fg)(\hat{x}) = \int_S u^\infty(\hat{x}, d) g(d) ds(d), \quad \hat{x} \in S. \quad (2.9)$$

Indeed, the connection between (2.7) and (2.9) is essentially based on the incident field  $u^i(x)$  and the far-field pattern  $u^\infty(\hat{x}, d)$ . Since  $v^i$  with the kernel  $g$  is the solution of (2.8), then by using the relationship between the boundary values of radiating solutions and their corresponding far-field pattern, we can obtain the integral equation of the first kind

$$Fg = \Phi^\infty(\hat{x}, z), \quad (2.10)$$

where  $\Phi^\infty(\hat{x}, z) = \frac{e^{i\pi/4}}{\sqrt{8\pi k}} e^{-ik\hat{x} \cdot z}$  is the far-field pattern of the fundamental solution  $\Phi(x, z)$ . The equation (2.10) is ill-posed, and hence the regularization scheme is required for solving  $g$ . Using the solved Herglotz kernel  $g$  in (2.10), the boundary point  $x \in \partial D$  can be determined from the non-linear equation

$$v^i(x) + \Phi(x, z) = 0. \quad (2.11)$$

Define the Herglotz operator  $H : L^2(S) \rightarrow L^2(\Lambda)$

$$(Hg)(x) = \int_S e^{ikx \cdot d} g(d) ds(d), \quad x \in \Lambda, \quad (2.12)$$

where  $\Lambda$  is the admissible surface in the suitable class  $U$ . The inverse obstacle scattering problem can be reformulated as an optimization problem with a regularization term using the cost function shown below:

$$\mathcal{J}(g, \Lambda; \alpha) := \|Fg - \Phi^\infty(\hat{x}, z)\|_{L^2(S)}^2 + \alpha \|Hg\|_{L^2(\Gamma)}^2 + \|Hg + \Phi(x, z)\|_{L^2(\Lambda)}^2, \quad (2.13)$$

where  $\Gamma$  is the  $C^2$ -surface which contains  $\Lambda$  in its interior and  $\alpha \in \mathbb{R}_+$  is the regularization parameter. We briefly mention here that the procedure described above is comparable to the Colton-Monk method presented in [10, 11, 12]. It is worth noting that (2.13) may work similarly to the neural network's loss function. This is the mathematical basis for creating a scattering-based network architecture in the following section.

**3. Deep decomposition method.** In this section, we propose a deep decomposition method (DDM) to approximate the inverse map  $\mathcal{G}^{-1}$  by creating a parametric map  $\mathcal{NN}_\theta$ , where  $\theta \in \Theta$  and  $\Theta$  is a finite dimensional parameter space. Furthermore, we will discuss its convergence result and discretization form.

**3.1. DDM for the inverse obstacle scattering problem.** DDM mainly consists of two parts, namely, the data retrieval and the boundary recovery. Therefore, in order to retrieve the full aperture data, a data completion network (DCnet) is designed in the first phase of DDM, that is

$$u_\theta^\infty(\hat{x}, d)|_{S \times S} = \text{DCnet}(u^\infty(\hat{x}, d)|_{\gamma^o \times \gamma^i}), \quad (3.1)$$

where  $u^\infty(\hat{x}, d)|_{\gamma^o \times \gamma^i}$  denoting  $u^\infty(\hat{x}, d)$  for  $(\hat{x}, d) \in \gamma^o \times \gamma^i$  is the input of DDM and  $u_\theta^\infty(\hat{x}, d)|_{S \times S}$  means the recovered  $u_\theta^\infty(\hat{x}, d)$  for  $(\hat{x}, d) \in S \times S$ . (3.1) can be done by minimizing the following functional

$$\mathcal{J}_{DC}(u_\theta^\infty(\hat{x}, d)) := \int_S \int_S |u^\infty(\hat{x}, d) - u_\theta^\infty(\hat{x}, d)|^2 ds(d) ds(\hat{x}). \quad (3.2)$$

After finding  $u_\theta^\infty(\hat{x}, d)$ , inspired by the preliminary results for the full aperture data, we further build a Herglotz kernel network named as HKnet for  $g$  and a boundary reconstruction network named as BRnet for  $\Lambda$  in the second phase of DDM. To do so, we first define a new far-field operator  $F_\theta : L^2(S) \rightarrow L^2(S)$

$$(F_\theta g)(\hat{x}) = \int_S u_\theta^\infty(\hat{x}, d) g_\theta(d) ds(d), \quad \hat{x} \in S, \quad (3.3)$$

where

$$g_\theta = \text{HKnet}(u_\theta^\infty(\hat{x}, d)|_{S \times S}). \quad (3.4)$$

Then, one can further have

$$\Lambda_\theta = \text{BRnet}(g_\theta), \quad (3.5)$$

where  $\Lambda_\theta$  is the final output of DDM. As seen in formulas (3.1), (3.4) and (3.5), in the DDM, the recovered  $u_\theta^\infty(\hat{x}, d)|_{S \times S}$  and  $g_\theta$  can be viewed as intermediate quantities. More specifically,  $u_\theta^\infty(\hat{x}, d)|_{S \times S}$  is not only the output of the DCnet but also the input of the HKnet, and  $g_\theta$  is not only the output of the HKnet but also the input of the BRnet. Analogous to (2.13), minimizing the cost functional

$$\mathcal{J}_{phy}(g_\theta, \Lambda_\theta; \alpha) := \|F_\theta g_\theta - \Phi^\infty(\hat{x}, z)\|_{L^2(S)}^2 + \alpha \|Hg_\theta\|_{L^2(\Gamma_\theta)}^2 + \|Hg_\theta + \Phi(x, z)\|_{L^2(\Lambda_\theta)}^2, \quad (3.6)$$

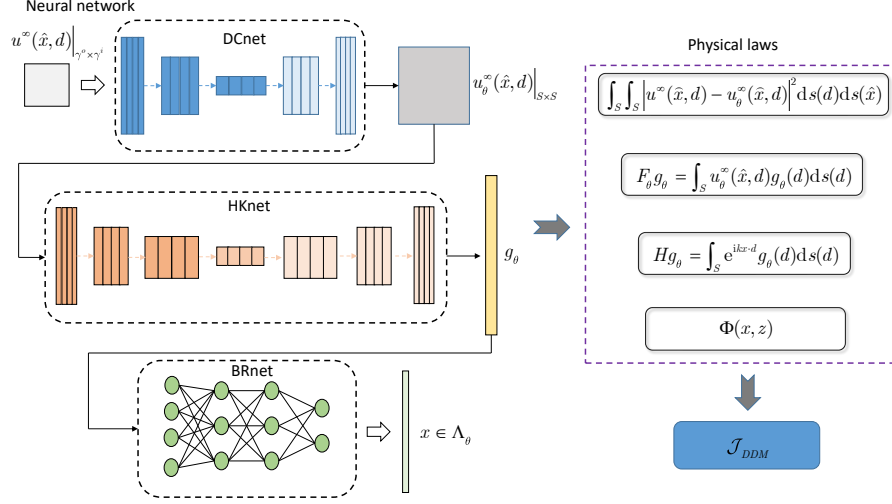


FIG. 3.1. A schematic illustration of DDM.

gives rise to  $g_\theta$  and  $\Lambda_\theta$ , where the  $C^2$ -surface  $\Gamma_\theta$  contains  $\Lambda_\theta$  in its interior.

In summary, the proposed DDM aims to minimize the combined cost functional

$$\mathcal{J}_{DDM}(u_\theta^\infty(\hat{x}, d), g_\theta, \Lambda_\theta; \alpha) = \mathcal{J}_{phy}(g_\theta, \Lambda_\theta; \alpha) + \beta_{DC} \mathcal{J}_{DC}(u_\theta^\infty(\hat{x}, d)), \quad (3.7)$$

for determining the optimal  $\Lambda_\theta^*$  by finding the optimal parameter  $\theta^* \in \Theta$ , and  $\beta_{DC}$  is a penalty factor that balances the physic-based loss  $\mathcal{J}_{phy}$  and the data-based loss  $\mathcal{J}_{DC}$ . The designed loss function (3.7) can well address both the nonlinearity and the ill-posedness caused by the inverse problem itself. From (3.1), (3.4) and (3.5), the parametric map  $\mathcal{NN}_\theta$  constructed by DDM for approximating the inverse operator can be summarized as

$$\mathcal{NN}_\theta = \text{BRnet}(\text{HKnet}(\text{DCnet})). \quad (3.8)$$

The general workflow of DDM is presented in Fig. 3.1.

**REMARK 3.1.** *As we have pointed out earlier, retrieving the full aperture data and recovering the boundary from given limited aperture data are addressed simultaneously in the learning stage of DDM, since the above proposed three networks are simultaneously trained and they share the same parameter  $\theta$ .*

**3.2. Convergence analysis.** We are going to investigate the convergence results of the DDM in this subsection. To this end, we first introduce the Herglotz wave function

$$v(x) = \int_S e^{ikx \cdot d} g(d) ds(d), \quad x \in \mathbb{R}^2, \quad (3.9)$$

which shares the same form of (2.7). Similarly to [10], we present the following definition of an optimal surface.

**DEFINITION 3.1.** *Given the (measured) limited aperture far-field  $u^\infty(\hat{x}, d) \in L^2(\gamma^o \times \gamma^i)$  and a regularization parameter  $\alpha \in \mathbb{R}_+$ , a boundary  $\Lambda_\theta^* \in U$  is called optimal if there exists a optimal  $u_{\theta^*}^\infty(\hat{x}, d) \in L^2(S \times S)$  such that*

$$\inf_{g_\theta \in L^2(S)} \mathcal{J}_{DDM}(u_{\theta^*}^\infty(\hat{x}, d), g_\theta, \Lambda_{\theta^*}; \alpha) = m(\alpha), \quad (3.10)$$

where

$$m(\alpha) = \inf_{u_\theta^\infty(\hat{x}, d) \in L^2(S \times S), g_\theta \in L^2(S), \Lambda_\theta \in U} \mathcal{J}_{DDM}(u_\theta^\infty(\hat{x}, d), g_\theta, \Lambda_\theta; \alpha),$$

$U$  is the compact admissible class and  $\theta^*$  is called the optimal parameter which shall be learned in the DDM.

The next two lemmas, which represent the convergence property of the cost functional and the existence of the optimal surface, respectively, are provided for the DDM convergence analysis.

LEMMA 3.1. *For each  $\alpha \in \mathbb{R}_+$ , there exists an optimal surface  $\Lambda_{\theta^*} \in U$ .*

*Proof.* Let  $(u_{\theta^n}^\infty(\hat{x}, d), g_{\theta^n}, \Lambda_{\theta^n})$  be a minimizing sequence from  $L^2(S \times S) \times L^2(S) \times U$ , that is,

$$\lim_{n \rightarrow \infty} \mathcal{J}_{DDM}(u_{\theta^n}^\infty(\hat{x}, d), g_{\theta^n}, \Lambda_{\theta^n}; \alpha) = m(\alpha).$$

Assume that  $\Lambda_{\theta^n} \rightarrow \Lambda_{\theta^*}$ ,  $n \rightarrow \infty$ , since  $U$  is compact. We can further assume that the sequence  $(Hg_{\theta^n})$  is weakly convergent in the space  $L^2(\Gamma_{\theta^n})$ , due to the following boundness

$$\alpha \|Hg_{\theta^n}\|_{L^2(\Gamma_{\theta^n})}^2 \leq \mathcal{J}_{DDM}(u_{\theta^n}^\infty(\hat{x}, d), g_{\theta^n}, \Lambda_{\theta^n}; \alpha) \rightarrow m(\alpha), \quad n \rightarrow \infty.$$

By Theorem 5.26 in [10], the weak convergence of the boundary data  $(Hg_{\theta^n})$  on  $\Gamma_{\theta^n}$  implies that the Herglotz wave functions  $v_n$  defined in (3.9) converge uniformly to a solution of the Helmholtz equation on the compact subsets of the interior of the surface  $\Gamma_{\theta^n}$  with the Herglotz kernel  $g_{\theta^n}$ . Then,

$$\lim_{n \rightarrow \infty} \|Hg_{\theta^n} + \Phi(x, z)\|_{L^2(\Lambda_{\theta^n})}^2 = \lim_{n \rightarrow \infty} \|Hg_{\theta^n} + \Phi(x, z)\|_{L^2(\Lambda_{\theta^*})}^2, \quad (3.11)$$

holds. Therefore, it is clear that

$$\lim_{n \rightarrow \infty} \mathcal{J}_{DDM}(u_{\theta^n}^\infty(\hat{x}, d), g_{\theta^n}, \Lambda_{\theta^n}; \alpha) = \lim_{n \rightarrow \infty} \mathcal{J}_{DDM}(u_{\theta^n}^\infty(\hat{x}, d), g_{\theta^n}, \Lambda_{\theta^*}; \alpha).$$

This completes the proof.  $\square$

LEMMA 3.2. *Let  $u^\infty(\hat{x}, d)$  be the exact far-field pattern of the obstacle  $D$  for all incident directions  $d$  such that  $\partial D$  belongs to  $U$ . Moreover, assume that given  $\varepsilon_1$  and  $\varepsilon_2$ , the recovered far-field pattern  $u_\theta^\infty(\hat{x}, d)$  and far-field operator  $F_\theta$  satisfy*

$$\|u^\infty(\hat{x}, d) - u_\theta^\infty(\hat{x}, d)\|_{L^2(S \times S)} < \varepsilon_1, \quad \|F - F_\theta\| < \varepsilon_2. \quad (3.12)$$

*Then, the functional  $m(\alpha)$  is convergent to zero when the parameter  $\alpha$  tends to zero, i.e.,*

$$\lim_{\alpha \rightarrow 0} m(\alpha) = 0. \quad (3.13)$$

*Proof.* Using Theorem 5.21 in [10] with given  $\varepsilon_3$ , there exists  $g_\theta \in L^2(S)$  which satisfies

$$\|Hg_\theta + \Phi(x, z)\|_{L^2(\partial D)} < \varepsilon_3.$$

Define a bounded and injective operator  $A : L^2(\partial D) \rightarrow L^2(S)$  mapping the boundary values of radiating solutions onto their corresponding far-field pattern. Then, it holds that

$$\|Fg_\theta - \Phi^\infty(\hat{x}, z)\|_{L^2(S)} \leq \|A\| \|Hg_\theta + \Phi(x, z)\|_{L^2(\partial D)}.$$

From (3.12), we further have

$$\begin{aligned} & \|F_\theta g_\theta - \Phi^\infty(\hat{x}, z)\|_{L^2(S)} \\ & \leq \|Fg_\theta - \Phi^\infty(\hat{x}, z)\|_{L^2(S)} + \|F_\theta g_\theta - Fg_\theta\|_{L^2(S)} \\ & \leq \|A\| \|Hg_\theta + \Phi(x, z)\|_{L^2(\partial D)} + \|F_\theta - F\| \|g_\theta\|_{L^2(S)} \\ & \leq \varepsilon_3 \|A\| + \varepsilon_2 \|g_\theta\|_{L^2(S)}. \end{aligned}$$

Using (3.12) again, we have

$$\begin{aligned} & \mathcal{J}_{DDM}(u_\theta^\infty(\hat{x}, d), g_\theta, \partial D; \alpha) \\ & \leq \beta_{DC} \varepsilon_1^2 + (\varepsilon_3 \|A\| + \varepsilon_2 \|g_\theta\|_{L^2(S)})^2 + \alpha \|Hg_\theta\|_{L^2(\Gamma_\theta)}^2 + \varepsilon_3^2 \\ & \rightarrow \beta_{DC} \varepsilon_1^2 + (\varepsilon_3 \|A\| + \varepsilon_2 \|g_\theta\|_{L^2(S)})^2 + \varepsilon_3^2, \quad \alpha \rightarrow 0. \end{aligned}$$

Since  $\varepsilon_1, \varepsilon_2$  and  $\varepsilon_3$  are arbitrary, (3.13) follows. This completes the proof.  $\square$

Now, we are ready to present the main convergence result.

**THEOREM 3.1.** *Let  $(\alpha_n)$  be a null sequence and  $(\Lambda_{\theta^n})$  be a corresponding sequence of optimal surfaces for the regularization parameter  $\alpha_n$ . Then, there exists a convergent subsequence of  $(\Lambda_{\theta^n})$ . Suppose that for all incident directions  $u^\infty(\hat{x}, d)$  is the exact far-field pattern of a sound-soft obstacle  $D$  such that  $\partial D$  belongs to the compact set  $U$ . For  $j \rightarrow \infty$ , the recovered far-field pattern  $u_{\theta^j}^\infty(\hat{x}, d)$  and far-field operator  $F_{\theta^j}$  are assumed to satisfy*

$$\|u^\infty(\hat{x}, d) - u_{\theta^j}^\infty(\hat{x}, d)\|_{L^2(S \times S)} \rightarrow 0, \quad \|F - F_{\theta^j}\| \rightarrow 0. \quad (3.14)$$

Furthermore, assume that the solution  $v^i$  to the associated interior Dirichlet problem (2.8) can be extended as a solution to the Helmholtz equation across the boundary  $\partial D$  into the interior of  $\Gamma_\theta$  with continuous boundary values on  $\Gamma_\theta$ . Then every limit point  $\Lambda_{\theta^*}$  of  $(\Lambda_{\theta^n})$  denotes the surface on which the boundary condition to the interior Dirichlet problem (2.8) is satisfied, that is,

$$v^i(x) + \Phi(x, z) = 0, \quad x \in \Lambda_{\theta^*}. \quad (3.15)$$

*Proof.* Because of the compactness of  $U$ , there exists a convergent subsequence of  $(\Lambda_{\theta^n})$ . Denote the limit point by  $\Lambda_{\theta^*}$ . Similarly, assume that  $\Lambda_{\theta^n} \rightarrow \Lambda_{\theta^*}, n \rightarrow \infty$ . By Theorem 5.21 in [10] and (2.7), there exists a sequence  $(g_{\theta^j})$  in  $L^2(S)$  satisfying

$$\|Hg_{\theta^j} - v^i\|_{L^2(\Gamma_{\theta^j})} \rightarrow 0, \quad j \rightarrow \infty. \quad (3.16)$$

Then, using Theorem 5.26 in [10], one can have that the Herglotz wave functions with the kernel  $g_{\theta^j}$  uniformly converge to  $v^i$  on the compact subsets of the interior of  $\Gamma_{\theta^j}$ . Furthermore, in view of the boundary condition in (2.8) for  $v^i$  on  $\partial D$ , we have

$$\|Hg_{\theta^j} + \Phi(x, z)\|_{L^2(\partial D)} \rightarrow 0, \quad j \rightarrow \infty. \quad (3.17)$$

Using the operator  $A : L^2(\partial D) \rightarrow L^2(S)$  mapping the boundary values of radiating solutions onto their corresponding far-field pattern, we further have

$$\|Fg_{\theta^j} - \Phi^\infty(\hat{x}, z)\|_{L^2(S)} \rightarrow 0, \quad j \rightarrow \infty. \quad (3.18)$$

Since  $\inf_{\Lambda_{\theta^j} \in U} \|Hg_{\theta^j} + \Phi(x, z)\|_{L^2(\Lambda_{\theta^j})}^2 \leq \|Hg_{\theta^j} + \Phi(x, z)\|_{L^2(\partial D)}^2$ , by the definition of  $m(\alpha)$  we can obtain

$$\begin{aligned} m(\alpha) &\leq \beta_{DC} \mathcal{J}_{DC}(u_{\theta^j}^\infty(\hat{x}, d)) + \|F_{\theta^j} g_{\theta^j} - \Phi^\infty(\hat{x}, z)\|_{L^2(S)}^2 \\ &\quad + \alpha \|Hg_{\theta^j}\|_{L^2(\Gamma_{\theta^j})}^2 + \|Hg_{\theta^j} + \Phi(x, z)\|_{L^2(\partial D)}^2 \\ &\leq \beta_{DC} \mathcal{J}_{DC}(u_{\theta^j}^\infty(\hat{x}, d)) + \|F_{\theta^j} g_{\theta^j} - \Phi^\infty(\hat{x}, z)\|_{L^2(S)}^2 \\ &\quad + \alpha \|Hg_{\theta^j} - v^i\|_{L^2(\Gamma_{\theta^j})}^2 + \alpha \|v^i\|_{L^2(\Gamma_{\theta^j})}^2 + \|Hg_{\theta^j} + \Phi(x, z)\|_{L^2(\partial D)}^2. \end{aligned} \quad (3.19)$$

Then for  $j \rightarrow \infty$  and all  $\alpha \in \mathbb{R}_+$ , combining (3.14) and (3.16)-(3.19) together gives rise to

$$m(\alpha) \leq \alpha \|v^i\|_{L^2(\Gamma_{\theta^j})}^2, \quad (3.20)$$

In addition, by Lemma 3.1, for each  $n$  there exists  $g_{\theta^n} \in L^2(S)$  satisfying

$$\mathcal{J}_{DDM}(u_{\theta^n}^\infty(\hat{x}, d), g_{\theta^n}, \Lambda_{\theta^n}; \alpha_n) \leq m(\alpha_n) + \alpha_n^2. \quad (3.21)$$

By (3.20), (3.21) and  $\alpha_n \|Hg_{\theta^n}\|_{L^2(\Gamma_{\theta^n})}^2 \leq \mathcal{J}_{DDM}(u_{\theta^n}^\infty(\hat{x}, d), g_{\theta^n}, \Lambda_{\theta^n}; \alpha_n)$ , for all  $n$  we have that

$$\|Hg_{\theta^n}\|_{L^2(\Gamma_{\theta^n})}^2 \leq \|v^i\|_{L^2(\Gamma_{\theta^n})}^2 + \alpha_n,$$



which implies that the sequence  $Hg_{\theta^n}$  is weakly convergent in  $L^2(\Gamma_{\theta^n})$ . Then, by Theorem 5.26 in [10], the Herglotz wave functions  $v_n$  with kernels  $g_{\theta^n}$  converge uniformly to the solution  $v^*$  of the Helmholtz equation on compact subsets of the interior of  $\Gamma_{\theta^n}$ . Moreover, by Lemma 3.2, we obtain  $m(\alpha_n) \rightarrow 0, n \rightarrow \infty$ . From (3.21), we also have

$$\|F_{\theta^n}g_{\theta^n} - \Phi^\infty(\hat{x}, z)\|_{L^2(S)}^2 \leq m(\alpha_n) + \alpha_n^2.$$

Therefore, there exists  $v_n$  which satisfies  $A(v_n + \Phi(x, z)) = Fg_{\theta^n} - \Phi^\infty(\hat{x}, z)$  for the boundary  $\partial D$ , then

$$\begin{aligned} & \|A(v_n + \Phi(x, z))\|_{L^2(S)} \\ &= \|Fg_{\theta^n} - \Phi^\infty(\hat{x}, z)\|_{L^2(S)}^2 \\ &\leq m(\alpha_n) + \alpha_n^2 + \|Fg_{\theta^n} - F_{\theta^n}g_{\theta^n}\|_{L^2(S)}^2. \end{aligned}$$

By (3.14), for  $n \rightarrow \infty$ , we have

$$\|A(v_n + \Phi(x, z))\|_{L^2(S)} \rightarrow 0,$$

and

$$A(v^* + \Phi(x, z)) = 0.$$

The fact in [10] that the operator  $A$  is injective yields

$$v^* + \Phi(x, z) = 0, \quad \text{on } \partial D. \quad (3.22)$$

From (2.8) and (3.22), we find that  $v^*$  and  $v^i$  have the same boundary condition on  $\partial D$ , implying that they possess the same Herglotz kernel. Therefore, one can further have  $v^i = v^*$  since  $k^2$  is assumed not to be the Dirichlet eigenvalue for the obstacle  $D$ . From (3.21), we obtain

$$\|v_n + \Phi(x, z)\|_{L^2(\Lambda_{\theta^n})}^2 \leq m(\alpha_n) + \alpha_n^2 \rightarrow 0, \quad n \rightarrow \infty, \quad (3.23)$$

which then gives rise to (3.15). This completes the proof.  $\square$

Under additional assumptions, we can further get the convergence towards the exact boundary of the obstacle.

**THEOREM 3.2.** *Assume that  $D$  is contained in a circle  $C_{r_b}$  of radius  $r_b$  such that  $0 < k < \frac{k_{01}}{r_b}$ , where  $k_{01}$  means the first zero of the Bessel function  $J_0$ . Then the sequence  $\{\Lambda_{\theta^n}\}$  only has one limit point  $\Lambda_{\theta^*}$ , which coincides with  $\partial D$ .*

*Proof.* Suppose that  $\Lambda_{\theta^1}, \Lambda_{\theta^2} \in U$  are distinct limit points of  $\{\Lambda_{\theta^n}\}$ , which are respectively related to two obstacles  $D_1, D_2$ . Define a non-empty domain  $D_{12} := D_1 \setminus (\overline{D_1} \cap \overline{D_2})$ , where  $D_{12} \subset C_{r_b} \setminus \overline{D}$ . By the Theorem 3.1,  $v^i(x) + \Phi(x, z)$  is an eigenfunction of the negative Laplacian in  $D_{12}$  with the Dirichlet eigenvalue  $k^2$ . For  $C_{r_b}$ , the smallest positive eigenvalue is  $\frac{k_{01}^2}{b^2}$ . Denote  $k_{D_{12}}^2$  the first positive eigenvalue of the negative Laplacian in  $D_{12}$ . Since  $D_{12} \subset C_{r_b}$ , we can get  $\frac{k_{01}^2}{b^2} < k_{D_{12}}^2$ . By the assumption  $0 < k < \frac{k_{01}}{r_b}$ , we further have  $k < k_{D_{12}}$ , this contradicts the monotonicity of the Dirichlet eigenvalues. Therefore, if  $0 < k < \frac{k_{01}}{r_b}$ , the sequence  $\{\Lambda_{\theta^n}\}$  only has one limit point  $\Lambda_{\theta^*}$ . Since  $D$  is contained in a circle  $C_{r_b}$  and  $v^i(x) + \Phi(x, z) = 0$  is also satisfied on the boundary  $\partial D$ , then the only one limit point is  $\Lambda_{\theta^*} = \partial D$ .  $\square$

**REMARK 3.2.** *The conditions (3.12) and (3.14) are theoretically attainable by the universal approximation theorem of the deep neural network. In fact, the subsequent numerical experiments also verify the convergence of DDM. Although we restrict ourselves to the limited aperture case, clearly, the methodology of DDM can be applied to the full aperture case in which DCnet, the condition (3.12) and the condition (3.14) are not required. Moreover, in the full aperture case, higher accuracy can be achieved because we do not need to deal with the approximation error generated by (3.2).*

**3.3. The discretization of DDM.** This section presents the discretization of DDM for the subsequent numerical computation. To this end, we first give the discretization of the exact full aperture data  $u^\infty(\hat{x}, d)|_{S \times S}$ , which is regarded as multi-static response matrix (MSRM)  $\mathbb{F}_f$ . Taking  $\tau_i := \frac{(i-1)\pi}{m}, i = 1, 2, \dots, 2m$ , we can determine the direction of the incident and observation by

$$d_i := (\cos \tau_i, \sin \tau_i), \quad i = 1, 2, \dots, 2m,$$

and

$$\hat{x}_j := (\cos \tau_j, \sin \tau_j), \quad j = 1, 2, \dots, 2m.$$

Thus, the corresponding MSRM is

$$\mathbb{F}_f = \begin{bmatrix} u^\infty(\hat{x}_1, d_1), u^\infty(\hat{x}_1, d_2), \dots, u^\infty(\hat{x}_1, d_{2m}) \\ u^\infty(\hat{x}_2, d_1), u^\infty(\hat{x}_2, d_2), \dots, u^\infty(\hat{x}_2, d_{2m}) \\ \vdots \quad \quad \quad \vdots \quad \quad \quad \vdots \quad \quad \quad \vdots \\ u^\infty(\hat{x}_{2m}, d_1), u^\infty(\hat{x}_{2m}, d_2), \dots, u^\infty(\hat{x}_{2m}, d_{2m}) \end{bmatrix}. \quad (3.24)$$

Denote the limited incident aperture  $\gamma^i$  and limited observation aperture  $\gamma^o$  by

$$\gamma^i := (\cos \psi, \sin \psi), \quad \psi \subseteq [0, 2\pi],$$

and

$$\gamma^o := (\cos \phi, \sin \phi), \quad \phi \subset [0, 2\pi].$$

Similar to MSRM, the discretization of the DDM input, which is the exact limited aperture data  $u^\infty(\hat{x}, d)|_{\gamma^o \times \gamma^i}$ , is defined as

$$\mathbb{F}_l = \begin{bmatrix} u^\infty(\hat{x}_{n^o}, d_{n^i}), u^\infty(\hat{x}_{n^o}, d_{n^i+1}), \dots, u^\infty(\hat{x}_{n^o}, d_{N^i}) \\ u^\infty(\hat{x}_{n^o+1}, d_{n^i}), u^\infty(\hat{x}_{n^o+1}, d_{n^i+1}), \dots, u^\infty(\hat{x}_{n^o+1}, d_{N^i}) \\ \vdots \quad \quad \quad \vdots \quad \quad \quad \vdots \quad \quad \quad \vdots \\ u^\infty(\hat{x}_{N^o}, d_{n^i}), u^\infty(\hat{x}_{N^o}, d_{n^i+1}), \dots, u^\infty(\hat{x}_{N^o}, d_{N^i}) \end{bmatrix}, \quad (3.25)$$

with the same step size  $\frac{\pi}{m}$ . For example, if  $\phi = [0, \pi]$  and  $\psi = [0, 2\pi]$ , then  $n^o = 1$ ,  $N^o = m$ ,  $n^i = 1$  and  $N^i = 2m$ . If  $\phi = [0, \pi/2]$  and  $\psi = [\pi/2, 3\pi/2]$ , then  $n^o = 1$ ,  $N^o = m/2$ ,  $n^i = m/2 + 1$  and  $N^i = 3m/2$ . In addition, the discretization of the recovered full aperture data  $u_\theta^\infty(\hat{x}, d)|_{S \times S}$  by DCnet is given by

$$\mathbb{F}_{\theta, f} = \begin{bmatrix} u_\theta^\infty(\hat{x}_1, d_1), u_\theta^\infty(\hat{x}_1, d_2), \dots, u_\theta^\infty(\hat{x}_1, d_{2m}) \\ u_\theta^\infty(\hat{x}_2, d_1), u_\theta^\infty(\hat{x}_2, d_2), \dots, u_\theta^\infty(\hat{x}_2, d_{2m}) \\ \vdots \quad \quad \quad \vdots \quad \quad \quad \vdots \quad \quad \quad \vdots \\ u_\theta^\infty(\hat{x}_{2m}, d_1), u_\theta^\infty(\hat{x}_{2m}, d_2), \dots, u_\theta^\infty(\hat{x}_{2m}, d_{2m}) \end{bmatrix}. \quad (3.26)$$

Therefore, using (3.24) and (3.26) for discretizing the functional (3.2) derives

$$\tilde{\mathcal{J}}_{DC}(\mathbb{F}_{\theta, f}) := \left(\frac{\pi}{m}\right)^2 \sum_{i=1}^{2m} \sum_{j=1}^{2m} |\mathbb{F}_f^{(ji)} - \mathbb{F}_{\theta, f}^{(ji)}|^2, \quad (3.27)$$

where

$$\mathbb{F}_f^{(ji)} = u^\infty(\hat{x}_j, d_i), \quad \mathbb{F}_{\theta, f}^{(ji)} = u_\theta^\infty(\hat{x}_j, d_i).$$

Next, we shall discretize the recovered Herglotz kernel  $g_\theta(d)$  and recovered surface  $\Lambda_\theta$ . Discretizing  $g_\theta(d)$  yields

$$\tilde{g}_\theta = \begin{bmatrix} g_\theta(d_1) \\ g_\theta(d_2) \\ \vdots \\ g_\theta(d_{2m}) \end{bmatrix}. \quad (3.28)$$

To work with  $\Lambda_\theta$  numerically, we assume  $\Lambda_\theta$  is a star-like surface with respect to the origin, which is defined by

$$\Lambda_\theta := e^{q_\theta(t)}(\text{cost}, \text{sint}), \quad t \in [0, 2\pi], \quad (3.29)$$

where  $q_\theta(t)$  is in the form of truncated fourier expansion

$$q(t) = \frac{q_0}{\sqrt{2\pi}} + \sum_{n=1}^{N_\Lambda} \left( \frac{a_n \cos(nt)}{n^s \sqrt{\pi}} + \frac{b_n \sin(nt)}{n^s \sqrt{\pi}} \right), \quad (3.30)$$

and  $N_\Lambda$  is the cut-off frequency,  $s$  controls the decreasing rate of the corresponding Fourier coefficients. Instead of directly expanding  $e^{q_\theta(t)}$ , the expansion form (3.30) is conducive to ensuring the back propagation of DDM. Note that  $\Lambda_\theta$  is uniquely determined by a finite set

$$Q_\theta = (q_0, a_1, b_1, a_2, b_2, \dots, a_{N_\Lambda}, b_{N_\Lambda}) \in \mathbb{R}^{2N_\Lambda+1}, \quad (3.31)$$

which implies that determining  $\Lambda_\theta$  is equivalent to determining  $Q_\theta$ . Let  $t_l := \frac{2(l-1)\pi}{N_t}$ ,  $l = 1, 2, \dots, N_t$ , where  $N_t$  is the number of surface discretization. Then, each boundary point  $x_{\Lambda_\theta}^{(l)} \in \Lambda_\theta$  is defined by

$$x_{\Lambda_\theta}^{(l)} := e^{q_\theta(t_l)}(\text{cost}_l, \text{sint}_l), \quad l = 1, 2, \dots, N_t. \quad (3.32)$$

Moreover, throughout the paper, to meet the above theoretical requirement, we set  $\Gamma_\theta = 1.001\Lambda_\theta$  to ensure that  $\Lambda_\theta$  is contained in the interior of  $\Gamma_\theta$ . Clearly, each point  $x_{\Gamma_\theta}^{(l)} \in \Gamma_\theta$  is  $x_{\Gamma_\theta}^{(l)} = 1.001x_{\Lambda_\theta}^{(l)}$ . Therefore, discretizing the functional (3.6) derives

$$\begin{aligned} & \tilde{\mathcal{J}}_{phy}(\tilde{g}_\theta, Q_\theta; \alpha) \\ & := \frac{\pi}{m} \sum_{j=1}^{2m} \left| \frac{\pi}{m} \sum_{i=1}^{2m} \mathbb{F}_{\theta, f}^{(ji)} \tilde{g}_\theta^{(i)} - \Phi^\infty(\hat{x}_j, z) \right|^2 \\ & + \alpha \frac{2\pi}{N_t} \sum_{l=1}^{N_t} \left| \frac{\pi}{m} \sum_{i=1}^{2m} e^{ikx_{\Gamma_\theta}^{(l)} \cdot d_i} \tilde{g}_\theta^{(i)} \right|^2 \\ & + \frac{2\pi}{N_t} \sum_{l=1}^{N_t} \left| \frac{\pi}{m} \sum_{i=1}^{2m} e^{ikx_{\Lambda_\theta}^{(l)} \cdot d_i} \tilde{g}_\theta^{(i)} + \Phi(x_{\Lambda_\theta}^{(l)}, z) \right|^2, \end{aligned} \quad (3.33)$$

where  $\tilde{g}_\theta^{(i)} = g_\theta(d_i)$ . We would like to point out that, the Jacobian terms  $e^{q_\theta(t_l)} \sqrt{1 + (q'_\theta(t_l))^2}$  and  $1.001e^{q_\theta(t_l)} \sqrt{1 + (q'_\theta(t_l))^2}$  are omitted in (3.33) for simplicity, which will not destroy the solution of the inverse problem. Finally, to learn  $\theta$  in DDM, we focus on minimizing

$$\tilde{\mathcal{J}}_{DDM}(\mathbb{F}_{\theta, f}, \tilde{g}_\theta, x_{\Lambda}^{(l)}; \alpha) = \tilde{\mathcal{J}}_{phy}(\tilde{g}_\theta, Q_\theta; \alpha) + \beta_{DC} \tilde{\mathcal{J}}_{DC}(\mathbb{F}_{\theta, f}). \quad (3.34)$$

The aforementioned discussions are based on the noise-free case. Next, we show that adding the relatively small noise to the input  $\mathbb{F}_l$  will promote DDM to learn more properties of the inverse

operator  $\mathcal{G}^{-1}$ . Since  $\mathbb{F}_{\theta,f}$ ,  $\tilde{g}_\theta$  and  $\Lambda_\theta$  are functions with respect to  $\mathbb{F}_l$ , we write  $\tilde{\mathcal{J}}_{DDM}(\mathbb{F}_l)$  to specify the dependence of DDM on the input  $\mathbb{F}_l$ . Let  $\mathbb{E}[\cdot]$  signify the expectation. To analyze the influence of the noise, we perturb the limited aperture data  $\mathbb{F}_l$  in the form

$$\mathbb{F}_{l,\eta} = \mathbb{F}_l + \eta, \quad (3.35)$$

where  $\mathbb{E}[\eta] = 0$  and the elements of  $\eta$  are independent of each other. Then the following theorem holds.

**THEOREM 3.3.** *Let  $\mathbb{F}_{l,\eta}$  be the noisy input defined in the form (3.35), then*

$$\mathbb{E}[\tilde{\mathcal{J}}_{DDM}(\mathbb{F}_{l,\eta})] = \tilde{\mathcal{J}}_{DDM}(\mathbb{F}_l) + \frac{1}{2} \sum_{j_1=n^o}^{N^o} \sum_{\tilde{j}_1=n^i}^{N^i} \frac{\partial^2 \tilde{\mathcal{J}}_{DDM}}{\partial \mathbb{F}_l^{(j_1 \tilde{j}_1)} \partial \mathbb{F}_l^{(j_1 \tilde{j}_1)}} \mathbb{E}[(\eta^{(j_1 \tilde{j}_1)})^2] + \mathbb{E}[o(\|\eta\|_F^2)], \quad (3.36)$$

where  $\eta^{(j^i)}$  is the element located at the  $j$ th row and the  $i$ th column of  $\eta$ , and  $\|\cdot\|_F$  is the Frobenius norm.

*Proof.* For  $\tilde{\mathcal{J}}_{DDM}(\mathbb{F}_{l,\eta})$ , we perform the Taylor expansion around  $\mathbb{F}_l$  up to second-order to get

$$\begin{aligned} \tilde{\mathcal{J}}_{DDM}(\mathbb{F}_{l,\eta}) &= \tilde{\mathcal{J}}_{DDM}(\mathbb{F}_l) + \sum_{j_1=n^o}^{N^o} \sum_{\tilde{j}_1=n^i}^{N^i} \frac{\partial \tilde{\mathcal{J}}_{DDM}}{\partial \mathbb{F}_l^{(j_1 \tilde{j}_1)}} \eta^{(j_1 \tilde{j}_1)} \\ &+ \frac{1}{2} \sum_{j_2=n^o}^{N^o} \sum_{\tilde{j}_2=n^i}^{N^i} \sum_{j_1=n^o}^{N^o} \sum_{\tilde{j}_1=n^i}^{N^i} \frac{\partial^2 \tilde{\mathcal{J}}_{DDM}}{\partial \mathbb{F}_l^{(j_2 \tilde{j}_2)} \partial \mathbb{F}_l^{(j_1 \tilde{j}_1)}} \eta^{(j_2 \tilde{j}_2)} \eta^{(j_1 \tilde{j}_1)} + o(\|\eta\|_F^2). \end{aligned}$$

Since  $\mathbb{E}[\eta] = 0$  and the elements of  $\eta$  are independent of each other, then it immediately follows that  $\mathbb{E}[\tilde{\mathcal{J}}_{DDM}(\mathbb{F}_{l,\eta})]$  is in the form (3.36).  $\square$

It is observed in (3.36) that  $\mathbb{E}[\tilde{\mathcal{J}}_{DDM}(\mathbb{F}_{l,\eta})]$  is the sum of the original loss  $\tilde{\mathcal{J}}_{DDM}(\mathbb{F}_l)$  and the induced regularization terms. These regularization terms deeply rely on  $\frac{\partial^2 \tilde{\mathcal{J}}_{DDM}}{\partial \mathbb{F}_l^{(j_1 \tilde{j}_1)} \partial \mathbb{F}_l^{(j_1 \tilde{j}_1)}}$ . Since  $\tilde{\mathcal{J}}_{DC}$  is mainly concerned with the data completion, we only need to focus on  $\frac{\partial^2 \tilde{\mathcal{J}}_{phy}}{\partial \mathbb{F}_l^{(j_1 \tilde{j}_1)} \partial \mathbb{F}_l^{(j_1 \tilde{j}_1)}}$ . Here,  $\frac{\partial^2 \tilde{\mathcal{J}}_{phy}}{\partial \mathbb{F}_l^{(j_1 \tilde{j}_1)} \partial \mathbb{F}_l^{(j_1 \tilde{j}_1)}}$  can be written as

$$\frac{\partial^2 \tilde{\mathcal{J}}_{phy}}{\partial \mathbb{F}_l^{(j_1 \tilde{j}_1)} \partial \mathbb{F}_l^{(j_1 \tilde{j}_1)}} = \mathcal{P}_1 + \mathcal{P}_2 + \mathcal{P}_3,$$

where

$$\begin{aligned} \mathcal{P}_1 &= \frac{2\pi}{m} \sum_{j=1}^{2m} \left( \frac{\pi}{m} \sum_{i=1}^{2m} \frac{\partial \mathbb{F}_{\theta,f}^{(j^i) \sim (i)} \tilde{g}_\theta}{\partial \mathbb{F}_l^{(j_1 \tilde{j}_1)}} \right)^2 \\ &+ \frac{2\pi}{m} \sum_{j=1}^{2m} \left( \frac{\pi}{m} \sum_{i=1}^{2m} \mathbb{F}_{\theta,f}^{(j^i) \sim (i)} - \Phi^\infty(\hat{x}_j, z) \right) \left( \frac{\pi}{m} \sum_{i=1}^{2m} \frac{\partial^2 \mathbb{F}_{\theta,f}^{(j^i) \sim (i)} \tilde{g}_\theta}{\partial \mathbb{F}_l^{(j_1 \tilde{j}_1)} \partial \mathbb{F}_l^{(j_1 \tilde{j}_1)}} \right), \\ \mathcal{P}_2 &= \alpha \frac{4\pi}{N_t} \sum_{l=1}^{N_t} \left( \frac{\pi}{m} \sum_{i=1}^{2m} \frac{\partial e^{ikx_{\Gamma_\theta}^{(l)} \cdot d_i \sim (i)} \tilde{g}_\theta}{\partial \mathbb{F}_l^{(j_1 \tilde{j}_1)}} \right)^2 \\ &+ \alpha \frac{4\pi}{N_t} \sum_{l=1}^{N_t} \left( \frac{\pi}{m} \sum_{i=1}^{2m} e^{ikx_{\Gamma_\theta}^{(l)} \cdot d_i \sim (i)} \tilde{g}_\theta \right) \left( \frac{\pi}{m} \sum_{i=1}^{2m} \frac{\partial^2 e^{ikx_{\Gamma_\theta}^{(l)} \cdot d_i \sim (i)} \tilde{g}_\theta}{\partial \mathbb{F}_l^{(j_1 \tilde{j}_1)} \partial \mathbb{F}_l^{(j_1 \tilde{j}_1)}} \right), \end{aligned}$$

and

$$\begin{aligned} \mathcal{P}_3 = & \frac{4\pi}{N_t} \sum_{l=1}^{N_t} \left( \frac{\partial \Phi(x_{\Lambda_\theta}^{(l)}, z)}{\partial \mathbb{F}_l^{(j_1 \tilde{j}_1)}} + \frac{\pi}{m} \sum_{i=1}^{2m} \frac{\partial e^{ikx_{\Lambda_\theta}^{(l)} \cdot d_i \tilde{g}_\theta^{(i)}}}{\partial \mathbb{F}_l^{(j_1 \tilde{j}_1)}} \right)^2 \\ & + \frac{4\pi}{N_t} \sum_{l=1}^{N_t} \left( \Phi(x_{\Lambda_\theta}^{(l)}, z) + \frac{\pi}{m} \sum_{i=1}^{2m} e^{ikx_{\Lambda_\theta}^{(l)} \cdot d_i \tilde{g}_\theta^{(i)}} \right) \left( \frac{\partial^2 \Phi(x_{\Lambda_\theta}^{(l)}, z)}{\partial \mathbb{F}_l^{(j_1 \tilde{j}_1)} \partial \mathbb{F}_l^{(j_1 \tilde{j}_1)}} + \frac{\pi}{m} \sum_{i=1}^{2m} \frac{\partial^2 e^{ikx_{\Lambda_\theta}^{(l)} \cdot d_i \tilde{g}_\theta^{(i)}}}{\partial \mathbb{F}_l^{(j_1 \tilde{j}_1)} \partial \mathbb{F}_l^{(j_1 \tilde{j}_1)}} \right). \end{aligned}$$

The original loss  $\tilde{\mathcal{J}}_{DDM}(\mathbb{F}_l)$  ensures that  $\Lambda_\theta$  is close to the boundary  $\partial D$ , as described in Theorem 3.2.  $\mathcal{P}_1$ ,  $\mathcal{P}_2$  and  $\mathcal{P}_3$  not only further strengthen this closeness, but also improve the smoothness of  $\mathbb{F}_{\theta, f}$ ,  $\tilde{g}_\theta$  and  $\Lambda_\theta$ . In addition,  $\mathcal{P}_3$  shows that the first derivative and the second derivative of  $\Phi(x_{\Lambda_\theta}^{(l)}, z) + \frac{\pi}{m} \sum_{i=1}^{2m} e^{ikx_{\Lambda_\theta}^{(l)} \cdot d_i \tilde{g}_\theta^{(i)}}$  are required to be small. Therefore, by adding the relatively small noise, the parametric map  $\mathcal{NN}_\theta$  is capable of approximating the inverse operator  $\mathcal{G}^{-1}$  up to the second derivative.

**4. Numerical experiments.** In this section, we will present numerical examples to show the effectiveness of DDM for the limited aperture inverse scattering problem (2.6).

**4.1. Experiment Setup.** In all the following examples, the noise  $\eta$  in (3.35) is generated by the formula

$$\eta = \sigma \Delta \mathbb{F}_l,$$

where  $\sigma$  refers to the noise level,  $\Delta$  is a random number drawn from the uniform distribution  $\mathcal{U}(-1, 1)$ .  $\mathbb{F}_l$  is generated by the boundary integral equation method with the single layer potential. Unless otherwise specified, we shall use the following parameters:  $k = 3$ ,  $m = 16$ ,  $N_t = 64$ ,  $N_\Lambda = 8$ ,  $s = 1$ ,  $\alpha = 10^{-8}$  and  $z = (0, 0)$ . Next, we introduce data generation and network structure for training DDM in detail.

**Data generation and Network structure.** To generate training and test samples, similar to (3.29)-(3.31), the boundary set  $\{\partial D^{(n_s)}\}_{n_s=1}^{N_s}$  is built by  $q_0^{(n_s)} \sim \mathcal{U}(0.5, 1.5)$ ,  $a_n^{(n_s)}, b_n^{(n_s)} \sim \mathcal{N}(0, 0.2)$ ,  $n = 1, 2, 3, 4$  and  $a_n^{(n_s)}, b_n^{(n_s)} \sim \mathcal{U}(0, 0.1)$ ,  $n = 5, 6, 7, 8$ . Here, the total number of samples  $N_s$  is chosen to be  $N_s = 5000$ .  $0.8N_s$  instances and  $0.2N_s$  instances are used for training and testing, respectively. Using the boundary integral equation method, one can further have a data of pairs  $\{\mathbb{F}_{l, \eta; n_s}, \mathbb{F}_{f; n_s}\}_{n_s=1}^{N_s}$  for training DDM, where  $\mathbb{F}_{l, \eta; n_s}$  denotes the  $n_s$ th noisy input sample and  $\mathbb{F}_{f; n_s}$  is the  $n_s$ th exact full aperture data. Clearly, note that DDM does not require the boundary set  $\{\partial D^{(n_s)}\}_{n_s=1}^{N_s}$  during the online training stage. Therefore, instead of using data pairs  $\{\mathbb{F}_{l, \eta; n_s}, \mathbb{F}_{f; n_s}, \partial D^{(n_s)}\}_{n_s=1}^{N_s}$  in purely data-driven networks, DDM employs  $\{\mathbb{F}_{l, \eta; n_s}, \mathbb{F}_{f; n_s}\}_{n_s=1}^{N_s}$  with underlying physical operators to effectively address the ill-posedness and well make itself interpretable.

Then, we introduce the network structures of DDM. The structure of DCnet is a feed-forward stack of four sequential combinations of the convolution, batch normalization and ReLU layers, followed by one fully connected layer. The number of filters in the four convolutional layers of DCnet are respectively 4, 8, 16 and 1. HKnet is a feed-forward stack consisting of four sequential combinations of the convolution, batch normalization and ReLU layers, followed by two fully connected layers. The number of filters in these four convolutional layers are 16, 32, 8 and 1, respectively. Furthermore, the two fully connected layers in HKnet have 512 and  $4m$  neurons, respectively. Finally, the architecture of BRnet consists of two fully connected layers, in which the number of neurons are 32 and  $2N_\Lambda + 1$ , respectively. In all the convolutional layers of DDM, one-stride, zero-padding and  $3 \times 3$  kernel are employed, as well as the biases are discarded. See Fig. 4.1 for the schematic illustration of the network structure of DDM in all the numerical examples.

**Loss function for a mini-batch.** With the above constructed structure of DDM, we train DDM using the Adam optimizer [23] for 800 epochs with an initial learning rate of 0.0002 which

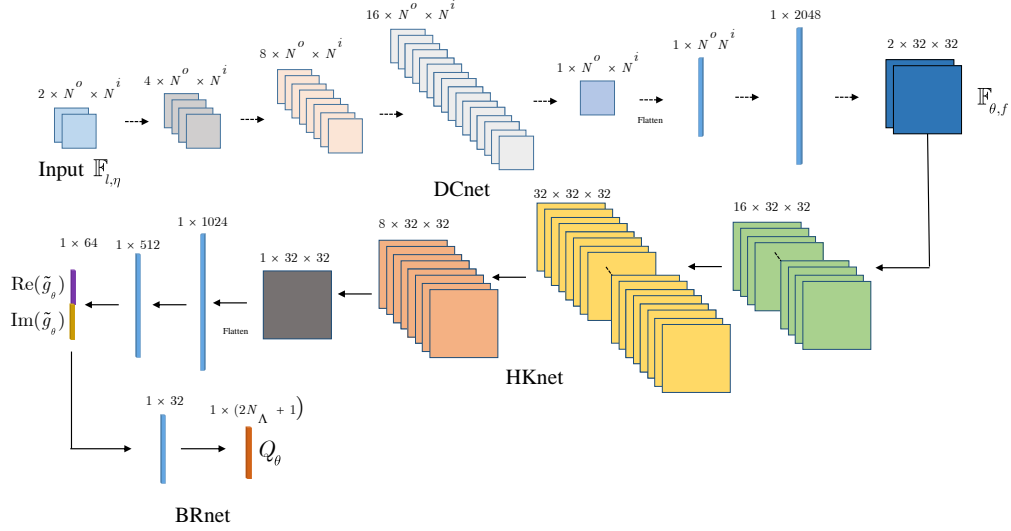


FIG. 4.1. A schematic illustration of the network structure of DDM in all the numerical examples.

is halved every 200 epochs. In addition, to learn  $\theta$ , a mini-batch of  $N_b$  samples are used in each iteration, where  $N_b \ll N_s$ . We set  $N_b = 64$ . Thus, the loss function  $\mathcal{L}_{DDM}$  for  $N_b$  samples in every iteration is defined as

$$\mathcal{L}_{DDM} = \mathcal{L}_{phy} + \beta_{DC} \mathcal{L}_{DC},$$

where

$$\mathcal{L}_{phy} := \frac{1}{N_b} \sum_{n_b=1}^{N_b} \tilde{\mathcal{J}}_{phy}(\tilde{g}_\theta^{(n_b)}, Q_\theta^{(n_b)}; \alpha), \quad \mathcal{L}_{DC} := \frac{1}{N_b} \sum_{n_b=1}^{N_b} \tilde{\mathcal{J}}_{DC}(\mathbb{F}_{\theta,f}^{(n_b)}).$$

For convenience, we set  $\beta_{DC} = 10$ .

**4.2. Numerical examples.** To demonstrate that DDM can recover complex scatterers, we will perform the following three types of examples:

- Case 1: best-case scenario: The boundary has the form described by (3.29) and (3.30). Specifically, the exact solution was selected at random from the following realizations:  $q_0 \sim \mathcal{U}(0.5, 1.5)$ ,  $a_n, b_n \sim \mathcal{N}(0, 0.2)$ ,  $n = 1, 2, 3, 4$  and  $a_n, b_n \sim \mathcal{U}(0, 0.1)$ ,  $n = 5, 6, 7, 8$ .
- Case 2: a pear-shaped obstacle. The boundary is parameterized as:

$$x(t) = (1.5 + 0.3 \sin 3t)(\cos t, \sin t), \quad 0 \leq t \leq 2\pi.$$

- Case 3: a rounded square-shaped obstacle. The boundary is parameterized as:

$$x(t) = \frac{3}{4}(\cos^3 t + \cos t, \sin^3 t + \sin t), \quad 0 \leq t \leq 2\pi.$$

Here, case 1 has the same distribution as the training set, and is used to detect in-distribution generalization. The last two scenarios, particularly the rounded square, are out of distribution. The pear-shaped obstacle is used to compare DDM reconstructions to those of the traditional Colton-Monk method in the star-like case. The rounded square-shaped obstacle is primarily used to test

generalization in the out-of-distribution case. For each of these examples, we also show the numerical results obtained using the direct sampling method (DSM) proposed in [31] for comparison, demonstrating the present approach’s fast computation and high-quality reconstructions. DSM is a popular method that is computationally efficient but only provides rough reconstructions. In this work, the indicator functional of DSM is

$$I(h) := |\varphi(h; -d) \mathbb{F}_{l,\sigma}^T \varphi^T(h; \hat{x})|,$$

where  $\varphi(h; -d) := (e^{-ikh \cdot d_{n^i}}, e^{-ikh \cdot d_{n^i+1}}, \dots, e^{-ikh \cdot d_{N^i}})$  and  $\varphi(h; \hat{x}) := (e^{ikh \cdot \hat{x}_{n^o}}, e^{ikh \cdot \hat{x}_{n^o+1}}, \dots, e^{ikh \cdot \hat{x}_{N^o}})$ . We set  $h \in V$ , where  $V$  is a grid of  $100 \times 100$  equally spaced sampling points on  $[-4, 4] \times [-4, 4]$ .

To demonstrate the superior performance of DDM, we numerically investigate its convergence property. The discrete relative error  $\text{Err}$  used to show convergence can be defined as follows:

$$\text{Err} = \frac{1}{N_b} \sum_{i=1}^{N_b} \frac{\|Q_\theta^{(i)} - Q_{true}^{(i)}\|_2^2}{\|Q_{true}^{(i)}\|_2^2},$$

where  $Q_{true}^{(i)}$  is the  $i$ th exact parameter set and  $Q_\theta^{(i)}$  is the  $i$ th recovered parameter set.

**Example 1: Different observation apertures.** In this example, we look at how the observation aperture affects the solution of the inverse problem using noise-free data. To this end, we set different observation apertures  $\phi = [0, \pi/2]$ ,  $\phi = [0, \pi]$  and  $\phi = [\pi/2, 3\pi/2]$ . The incident aperture is given by  $\psi = [0, 2\pi]$ .

Fig. 4.2 shows the relative error  $\text{Err}$ , the loss functions  $\mathcal{L}_{DDM}$ , and  $\mathcal{L}_{phy}$ . As shown in Fig. 4.2(c), the predicted  $\Lambda_\theta$  gradually converges to the exact boundary  $\partial D$  during the training process, which confirms to Theorem 3.2. Besides, Fig. 4.2 shows that the narrower observation aperture will lead to the larger loss functions and relative error. The recovered real parts of three obstacles for  $\phi = [0, \pi/2]$ ,  $\phi = [0, \pi]$  and  $\phi = [\pi/2, 3\pi/2]$  are shown in Fig. 4.3. The corresponding recovered imaginary parts are shown in Fig. 4.4. We find that the far-field data of these three obstacles is accurately recovered especially for  $\phi = [0, \pi]$  and  $\phi = [\pi/2, 3\pi/2]$ . This phenomenon occurs due to the fact that, in such two cases, there is more information that can be utilized. The far-field data can also be recovered to a certain satisfactory level for  $\phi = [0, \pi/2]$ . The boundary reconstructions by DDM for  $\phi = [0, \pi/2]$ ,  $\phi = [0, \pi]$  and  $\phi = [\pi/2, 3\pi/2]$  are presented in Fig. 4.5. For the comparison, the reconstructions by DSM are shown in Fig. 4.6. It is obvious that our DDM can provide satisfactory reconstructions even for the case of  $\phi = [0, \pi/2]$ , but only illuminated part of  $\partial D$  can be well recovered by DSM. This is reasonable because a deep learning based data retrieval called DCnet is deployed in DDM, and hence DDM can maintain high inversion quality for the limited observation aperture case. It is also noticed in Fig. 4.6 that the reconstructions are further distorted when the observation aperture becomes smaller. Moreover, compared to results in [20] by the classical Colton-Monk method, DDM can obtain higher reconstruction accuracy and require very little computational cost. As expected, the reconstructions of traditional inversion methods are deeply influenced by the limited aperture data, but DDM can well overcome this issue.

**Example 2: Different noise levels.** The influence of the noise level  $\sigma$  is considered in this example. To do so, we set the different noise levels  $\sigma = 0.02$ ,  $\sigma = 0.1$  and  $\sigma = 0.5$ . The observation aperture and the incident aperture are, respectively,  $\phi = [0, \pi/2]$  and  $\psi = [0, 2\pi]$ .

We first present loss functions  $\mathcal{L}_{DDM}$ ,  $\mathcal{L}_{phy}$  and the relative error  $\text{Err}$  in Fig.4.7. The convergence nature is theoretically prove in the noise free case, nonetheless, we find that DDM is also capable of converging to the exact boundary  $\partial D$  for the noisy case. Furthermore, as the noise level  $\sigma$  increases, the relative error shall become large, which is reasonable because the larger noise will bring more uncertainties. The recovered real parts of three obstacles for  $\sigma = 0.02$ ,  $\sigma = 0.1$  and  $\sigma = 0.5$  are plotted in Fig. 4.8, and the recovered imaginary parts are presented in Fig. 4.9. It is noted that even for the noise level  $\sigma = 0.5$ , DDM also can effectively recover the far-field data. The boundary reconstructions by DDM with  $\sigma = 0.02$ ,  $\sigma = 0.1$  and  $\sigma = 0.5$  are shown in Fig. 4.10. Similarly, we plot the reconstructions of DSM in Fig. 4.11 for the comparison. According to these figures, DDM

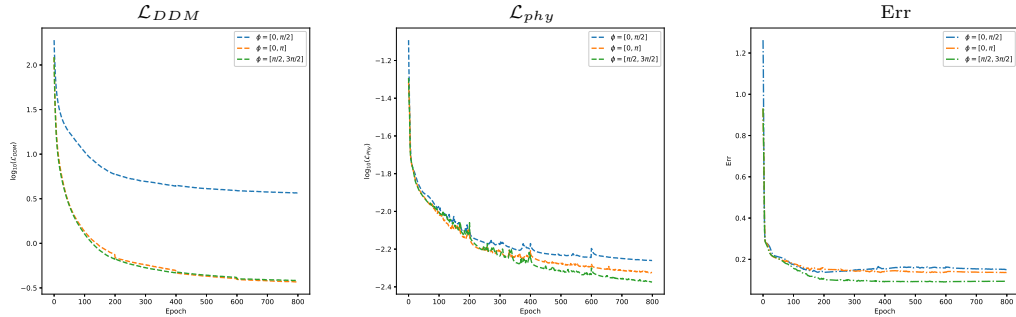


FIG. 4.2. The loss function  $\mathcal{L}_{DDM}$  (left), the loss function  $\mathcal{L}_{phy}$  (middle) and the relative error  $Err$  (right) for Example 1.

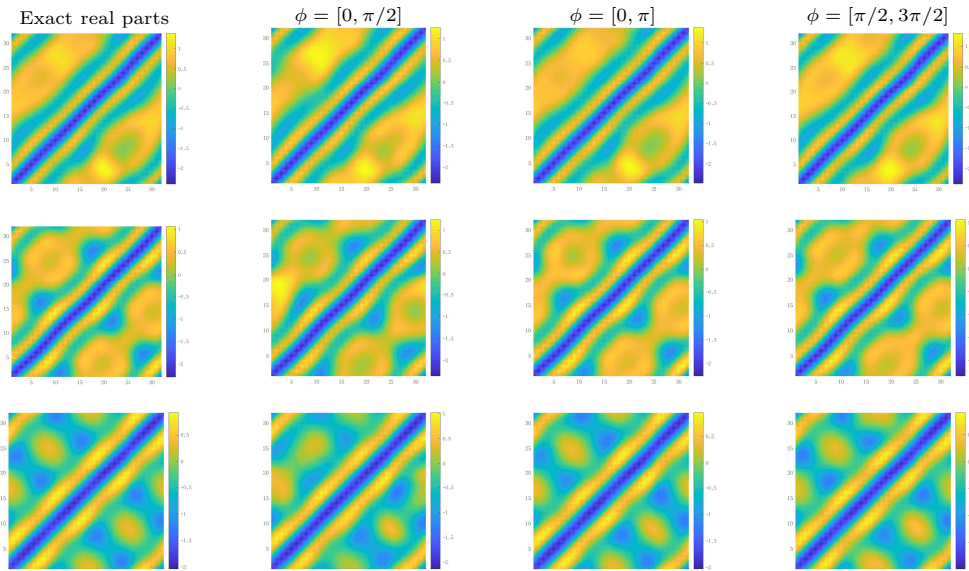


FIG. 4.3. The real parts of obstacles using observation apertures. Case 1: best-case scenario (Top), Case 2: a pear-shaped obstacle (middle) and Case 3: a rounded square-shaped obstacle (bottom).

is very robust to observational noise. This is possible owing to the reason that the recovered far-field data is integrated into the far-field operator (3.3), and hence to some extent the added noise can be alleviated. Although DSM is robust to noise, as shown in Fig. 4.11, its results are still influenced by the limited aperture data.

**Example 3: Different incident apertures.** In the above two examples, we only consider that the observation aperture is limited. However, the incident aperture is additionally limited in many real-world scenarios. Thus, the effect of the incident aperture is considered in this example. We set the different incident apertures  $\psi = [0, \pi]$ ,  $\psi = [\pi/2, 3\pi/2]$  and  $\psi = [\pi, 2\pi]$ . The observation aperture is  $\phi = [0, \pi/2]$  and the noise level is  $\sigma = 0.1$ . We would like to emphasize that the considered incident aperture and the observation aperture are both extremely limited, which shall make the inverse problem more challenging. Furthermore, in practice, the measured or computed data is typically noisy, which promotes us to also perturb the full aperture data by the same form

$$\mathbb{F}_{f, \eta_f} = \mathbb{F}_f + \eta_f,$$

where  $\eta_f = \sigma \Delta \mathbb{F}_f$ . From [2] we know that the noise added to the output of the neural network only



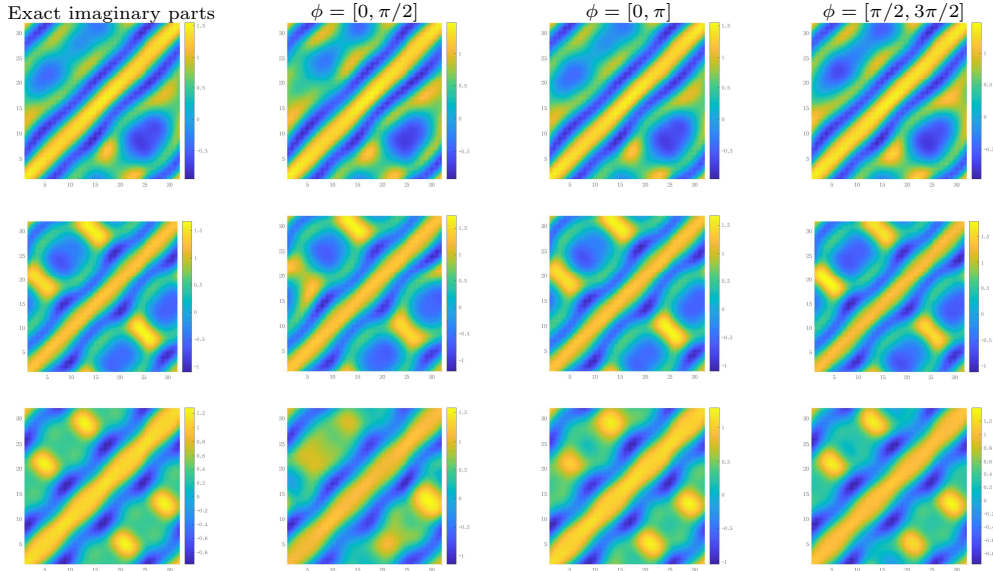


FIG. 4.4. The imaginary parts of obstacles using observation apertures. Case 1: best-case scenario (Top), Case 2: a pear-shaped obstacle (middle) and Case 3: a rounded square-shaped obstacle (bottom).

changes the loss function by a constant. Therefore, in this example, we use  $\{\mathbb{F}_{l,\eta;n_s}, \mathbb{F}_{f,\eta_f;n_s}\}_{n_s=1}^{N_s}$  to learn the inverse operator.

The loss functions  $\mathcal{L}_{DDM}$ ,  $\mathcal{L}_{phy}$  and the relative error Err of DDM are displayed in Fig. 4.12. It is clearly shown in Fig. 4.12(c) that DDM can gradually approximate the exact boundary  $\partial D$  for the situation that the incident and observation aperture are both limited. In Fig. 4.13, we show the recovered real parts of three obstacles, while Fig. 4.14 shows their recovered imaginary parts. The figures show that DDM can recover far-field data for  $\psi = [0, \pi]$ . However, for  $\psi = [\pi/2, 3\pi/2]$  and  $\psi = [\pi, 2\pi]$ , the recovered far-field data loses some accuracy. Figures 4.15 and 4.16 show the boundary reconstructions of DDM and DSM, respectively. It is observed that DDM can reconstruct the boundaries of the three obstacles with satisfactory inversion quality, whereas DSM is completely ineffective in this example because the limited observation data can only provide little physical and geometric information. Furthermore, we discovered that even when the aperture size is the same but the direction is different, the reconstruction results are still affected.

**5. Summary.** In this paper, we propose the deep decomposition method (DDM), a scattering-based neural network for determining the shape of a sound-soft obstacle from limited aperture data at a fixed wavenumber or frequency. In DDM, a data completion scheme based on deep learning is implemented to prevent any distortion of the reconstructions. On the other hand, we incorporate the scattering information, such as the far-field operator, the Herglotz operator, and the fundamental solution, into the loss function of DDM for the boundary recovery in order to better utilize the underlying physics information for learning the regularized inverse operator. Because physical information is present, DDM does not require exact shape data during the training stage. Moreover, DDM is a physics-aware machine learning method that can handle ill-posedness in addition to having interpretability. The convergence of DDM is demonstrated, and numerical examples are provided to illustrate the validity of DDM.

Our methodology in this work can be directly extended to other boundary condition cases, the inhomogeneous medium case and even the three-dimensional case. Using multifrequency data to construct the loss function of the scattering-based neural network is also a practical and interesting direction, which shall broaden the detectable range. Furthermore, because the data retrieval component of DDM is entirely data-driven, it is worthwhile to develop a physics-driven data completion

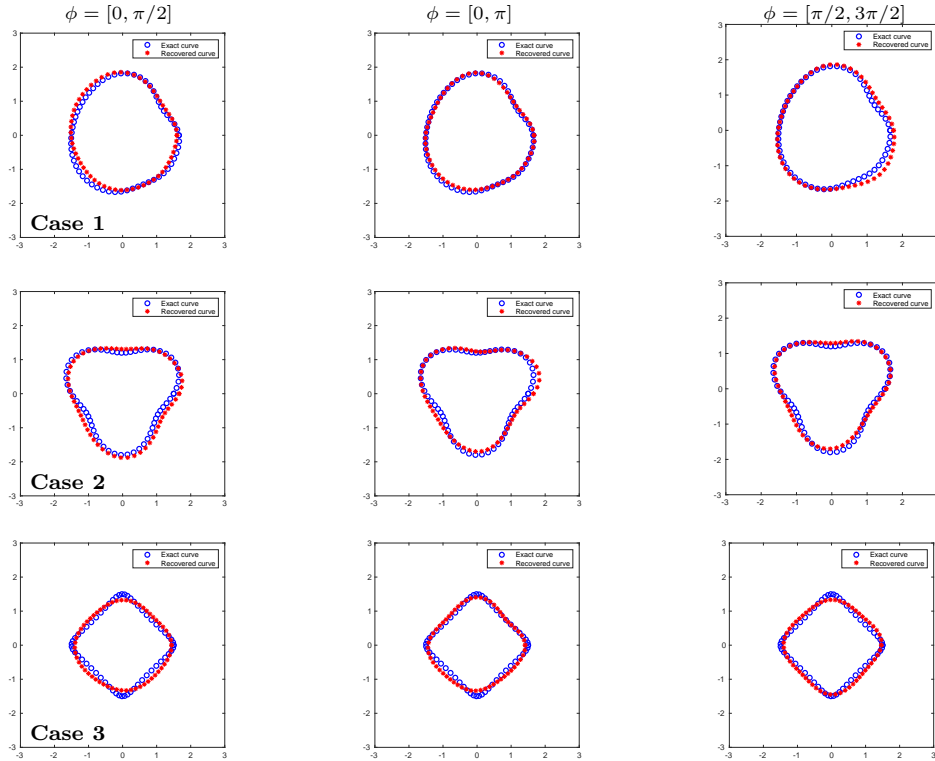


FIG. 4.5. Reconstructions made by DDM using observation apertures: best-case scenario (Top), a pear-shaped obstacle (middle) and a rounded square-shaped obstacle (bottom).

deep learning. These extensions will be considered in future works.

#### REFERENCES

- [1] H. Ammari, G. Bao, and J. Fleming. An inverse source problem for maxwell's equations in magnetoencephalography. *SIAM Journal on Applied Mathematics*, 62(4):1369–1382, 2002.
- [2] G. An. The effects of adding noise during backpropagation training on a generalization performance. *Neural computation*, 8(3):643–674, 1996.
- [3] L. Audibert and H. Haddar. The generalized linear sampling method for limited aperture measurements. *SIAM Journal on Imaging Sciences*, 10(2):845–870, 2017.
- [4] G. Bao, P. Li, J. Lin, and F. Triki. Inverse scattering problems with multi-frequencies. *Inverse Problems*, 31(9):093001, 2015.
- [5] G. Bao and J. Liu. Numerical solution of inverse scattering problems with multi-experimental limited aperture data. *SIAM Journal on Scientific Computing*, 25(3):1102–1117, 2003.
- [6] G. Bao, S. Lu, W. Rundell, and B. Xu. A recursive algorithm for multifrequency acoustic inverse source problems. *SIAM Journal on Numerical Analysis*, 53(3):1608–1628, 2015.
- [7] G. Bao, X. Ye, Y. Zang, and H. Zhou. Numerical solution of inverse problems by weak adversarial networks. *Inverse Problems*, 36(11):115003, 2020.
- [8] B. Borden. Mathematical problems in radar inverse scattering. *Inverse Problems*, 18(1):R1, 2001.
- [9] D. Colton and A. Kirsch. A simple method for solving inverse scattering problems in the resonance region. *Inverse problems*, 12(4):383–393, 1996.
- [10] D. Colton and R. Kress. *Inverse Acoustic and Electromagnetic Scattering Theory*. Springer, New York, 2019.
- [11] D. Colton and P. Monk. A novel method for solving the inverse scattering problem for time-harmonic acoustic waves in the resonance region. *SIAM journal on applied mathematics*, 45(6):1039–1053, 1985.
- [12] D. Colton and P. Monk. A novel method for solving the inverse scattering problem for time-harmonic acoustic waves in the resonance region ii. *SIAM journal on applied mathematics*, 46(3):506–523, 1986.
- [13] D. Colton, M. Piana, and R. Potthast. A simple method using morozov's discrepancy principle for solving inverse scattering problems. *Inverse problems*, 13(6):1477–1493, 1997.
- [14] F. Dou, X. Liu, S. Meng, and B. Zhang. Data completion algorithms and their applications in inverse acoustic

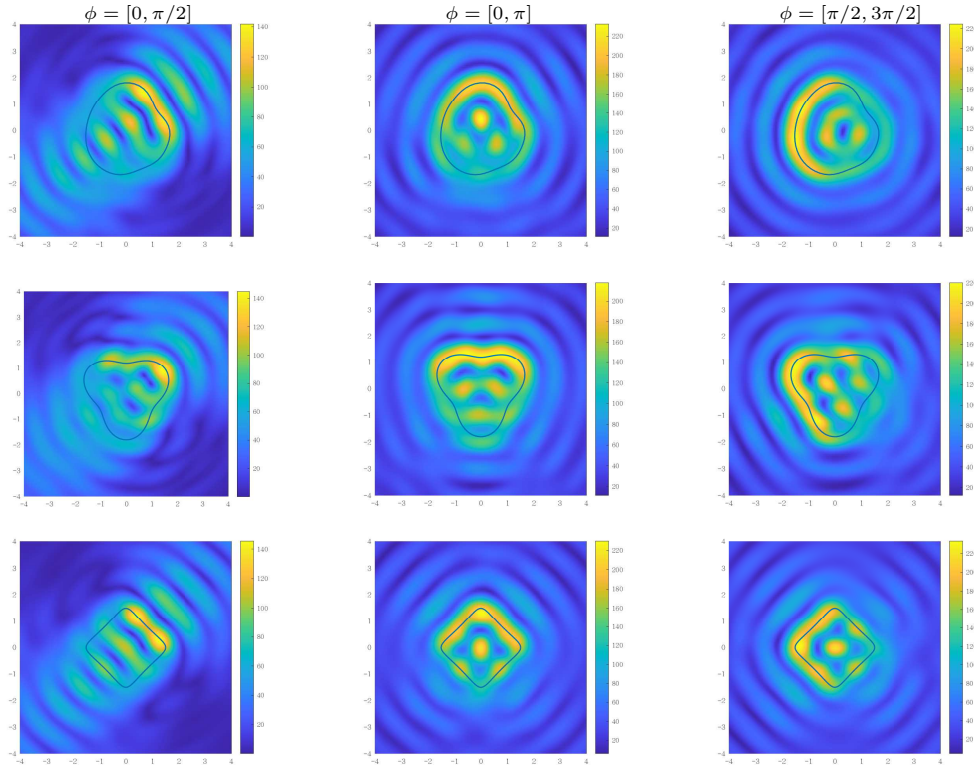


FIG. 4.6. Reconstructions made by DSM using observation apertures: best-case scenario (Top), a pear-shaped obstacle (middle) and a rounded square-shaped obstacle (bottom).

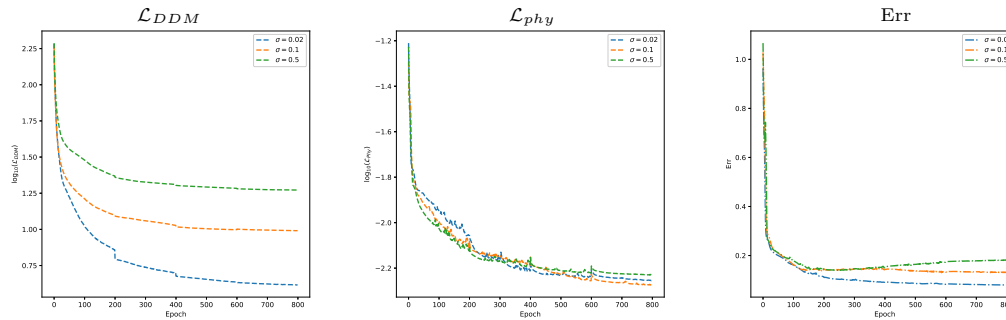


FIG. 4.7. The loss function  $\mathcal{L}_{DDM}$  (left), the loss function  $\mathcal{L}_{phy}$  (middle) and the relative error Err (right) for Example 2.

- scattering with limited-aperture backscattering data. *Journal of Computational Physics*, 469:111550, 2022.
- [15] Y. Gao, H. Liu, X. Wang, and K. Zhang. On an artificial neural network for inverse scattering problems. *Journal of Computational Physics*, 448:110771, 2022.
- [16] Y. Gao and K. Zhang. Machine learning based data retrieval for inverse scattering problems with incomplete data. *Journal of Inverse and Ill-Posed Problems*, 29(2):249–266, 2021.
- [17] T. Hohage. Convergence rates of a regularized newton method in sound-hard inverse scattering. *SIAM journal on numerical analysis*, 36(1):125–142, 1998.
- [18] M. Ikehata, E. Niemi, and S. Siltanen. Inverse obstacle scattering with limited-aperture data. *Inverse problems and imaging*, 2012.
- [19] K. Ito, B. Jin, and J. Zou. A direct sampling method to an inverse medium scattering problem. *Inverse Problems*, 28(2):025003, 2012.

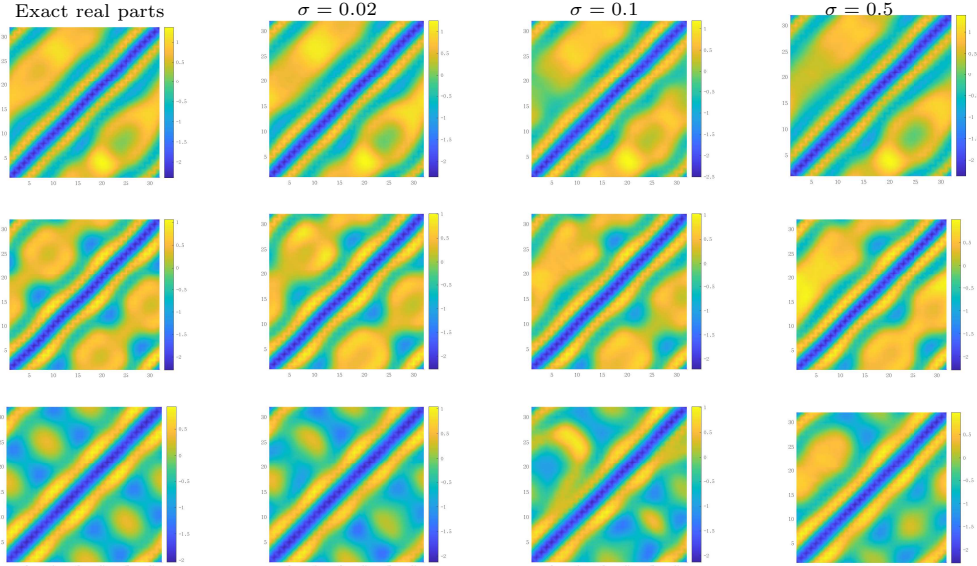


FIG. 4.8. The real parts of obstacles using various noise levels. Case 1: best-case scenario (Top), Case 2: a pear-shaped obstacle (middle) and Case 3: a rounded square-shaped obstacle (bottom).

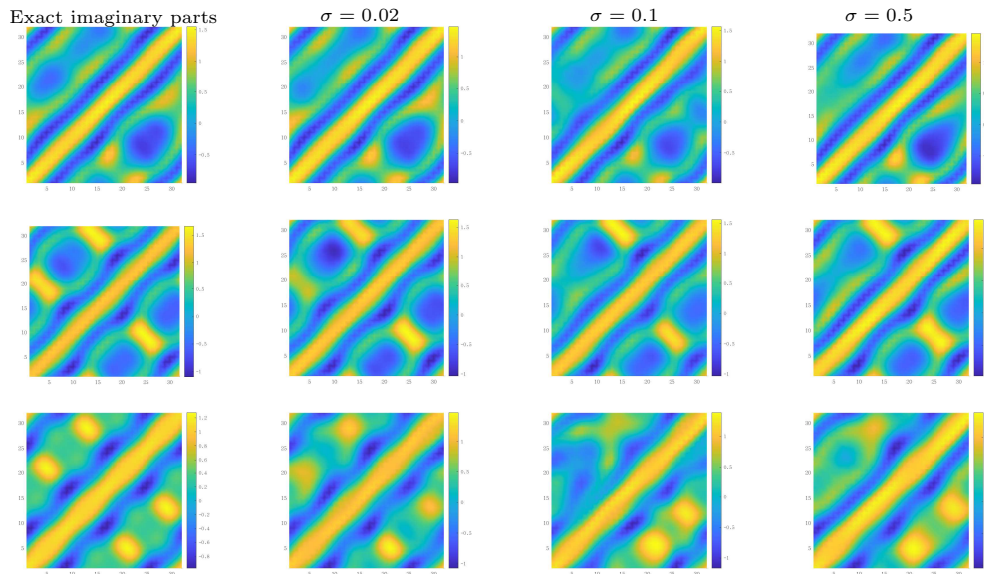


FIG. 4.9. The imaginary parts of obstacles using various noise levels. Case 1: best-case scenario (Top), Case 2: a pear-shaped obstacle (middle) and Case 3: a rounded square-shaped obstacle (bottom).

- [20] L. Robert J. Ochs. The limited aperture problem of inverse acoustic scattering: Dirichlet boundary conditions. *SIAM Journal on Applied Mathematics*, 47(6):1320–1341, 1987.
- [21] R.L. Ochs Jr. The limited aperture problem of inverse acoustic scattering: Dirichlet boundary conditions. *SIAM Journal on Applied Mathematics*, 47(6):1320–1341, 1987.
- [22] Y. Khoo and L. Ying. Switchnet: a neural network model for forward and inverse scattering problems. *SIAM Journal on Scientific Computing*, 41(5):A3182–A3201, 2019.
- [23] D. P. Kingma and J. Ba. Adam. A method for stochastic optimization. *arXiv preprint arXiv:1412.6980*, 1412, 2014.
- [24] A. Kirsch and R. Kress. An optimization method in inverse acoustic scattering. *Boundary Elements IX, vol. 3: Fluid flow and potential applications*, ed C.A. Brebbia et al, Berlin, Springer,, pages 3–18, 1987.

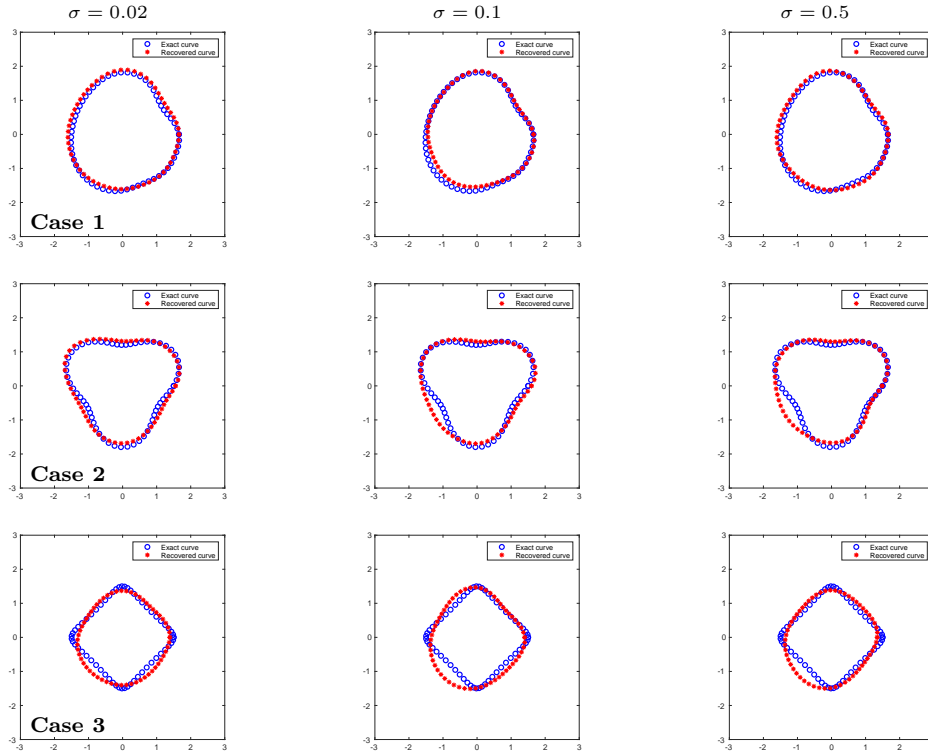


FIG. 4.10. Reconstructions made by DDM using various noise levels: best-case scenario (Top), a pear-shaped obstacle (middle) and a rounded square-shaped obstacle (bottom).

- [25] A. Kirsch and X. Liu. A modification of the factorization method for the classical acoustic inverse scattering problems. *Inverse Problems*, 30(3):035013, 2014.
- [26] R. Kress. Newtons method for inverse obstacle scattering meets the method of least squares. *Inverse Problems*, 19(6):91–104, 2003.
- [27] P. Kuchment. The radon transform and medical imaging. *CBMS-NSF Regional Conference Series in Applied Mathematics, Society for Industrial and Applied Mathematics*, 2014.
- [28] J. Li, H. Liu, W. Tsui, and X. Wang. An inverse scattering approach for geometric body generation: A machine learning perspective. *Mathematics in Engineering*, 1(4):800–823, 2019.
- [29] J. Li and J. Zou. A direct sampling method for inverse scattering using far-field data. *Inverse Problems and Imaging*, 7(1):757–775, 2013.
- [30] K. Li, B. Zhang, and H. Zhang. Reconstruction of inhomogeneous media by iterative reconstruction algorithm with learned projector. *arXiv preprint arXiv:2207.13032*, 2022.
- [31] X. Liu. A novel sampling method for multiple multiscale targets from scattering amplitudes at a fixed frequency. *Inverse Problems*, 33(8):085011, 2017.
- [32] X. Liu and J. Sun. Data recovery in inverse scattering: from limited-aperture to full-aperture. *Journal of Computational Physics*, 386:350–364, 2019.
- [33] L. Lu, R. Pestourie, W. Yao, Z. Wang, F. Verdugo, and S. G. Johnson. Physics-informed neural networks with hard constraints for inverse design. *SIAM Journal on Scientific Computing*, 43(6):B1105–B1132, 2021.
- [34] W. McLean. *Strongly elliptic systems and boundary integral equations*. Cambridge university press, 2000.
- [35] R. Molinaro, Y. Yang, B. Engquist, and S. Mishra. Neural inverse operators for solving pde inverse problems. *arXiv preprint arXiv:2301.11167*, 2023.
- [36] H V. Nguyen and T. Bui-Thanh. Tnet: A model-constrained tikhonov network approach for inverse problems. *SIAM Journal on Scientific Computing*, 46(1):C77–C100, 2024.
- [37] J. Ning, F. Han, and J. Zou. A direct sampling-based deep learning approach for inverse medium scattering problems. *Inverse Problems*, 40(1):015005, 2023.
- [38] J. Ning, F. Han, and J. Zou. A direct sampling method and its integration with deep learning for inverse scattering problems with phaseless data. *arXiv preprint arXiv:2403.02584*, 2024.
- [39] G A. Padmanabha and N. Zabaras. Solving inverse problems using conditional invertible neural networks. *Journal of Computational Physics*, 433:110194, 2021.
- [40] S. Pakravan, P. A. Mistani, M. A. Aragon-Calvo, and F. Gibou. Solving inverse-pde problems with physics-aware

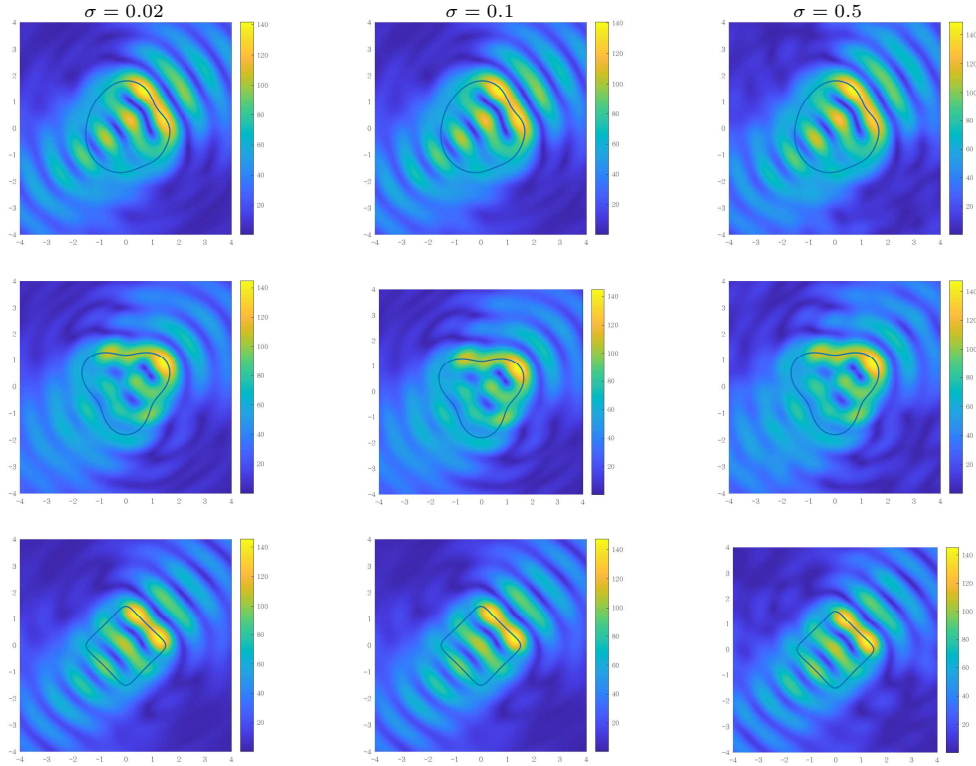


FIG. 4.11. Reconstructions made by DSM using various noise levels: best-case scenario (Top), a pear-shaped obstacle (middle) and a rounded square-shaped obstacle (bottom).

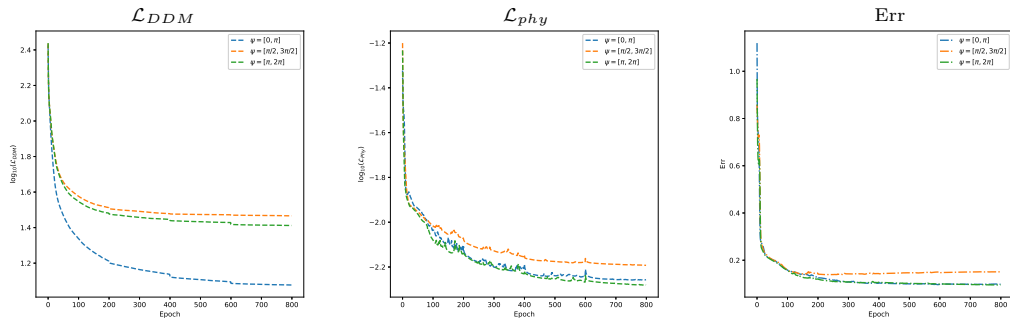


FIG. 4.12. The loss function  $\mathcal{L}_{DDM}$  (left), the loss function  $\mathcal{L}_{phy}$  (middle) and the relative error Err (right) for Example 3.

neural networks. *Journal of Computational Physics*, 440:110414, 2021.

- [41] M. Raissi, P. Perdikaris, and G. E. Karniadakis. Physics-informed neural networks: A deep learning framework for solving forward and inverse problems involving nonlinear partial differential equations. *Journal of Computational physics*, 378:686–707, 2019.
- [42] M. Rasht-Behesht, C. Huber, K. Shukla, and G. E. Karniadakis. Physics-informed neural networks (pinns) for wave propagation and full waveform inversions. *Journal of Geophysical Research: Solid Earth*, 127(5):e2021JB023120, 2022.
- [43] J. Yang, B. Zhang, and H. Zhang. Reconstruction of complex obstacles with generalized impedance boundary conditions from far-field data. *SIAM Journal on Applied Mathematics*, 74(1):106–124, 2014.
- [44] W. Yin, W. Yang, and H. Liu. A neural network scheme for recovering scattering obstacles with limited phaseless far-field data. *Journal of Computational Physics*, 417:109594, 2020.

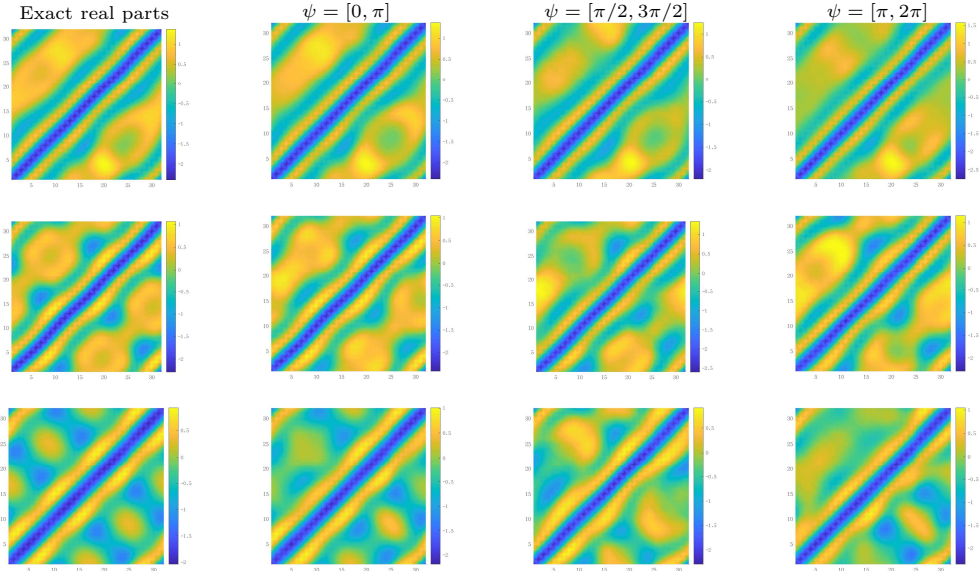


FIG. 4.13. The real parts of obstacles using various incident apertures. Case 1: best-case scenario (Top), Case 2: a pear-shaped obstacle (middle) and Case 3: a rounded square-shaped obstacle (bottom).

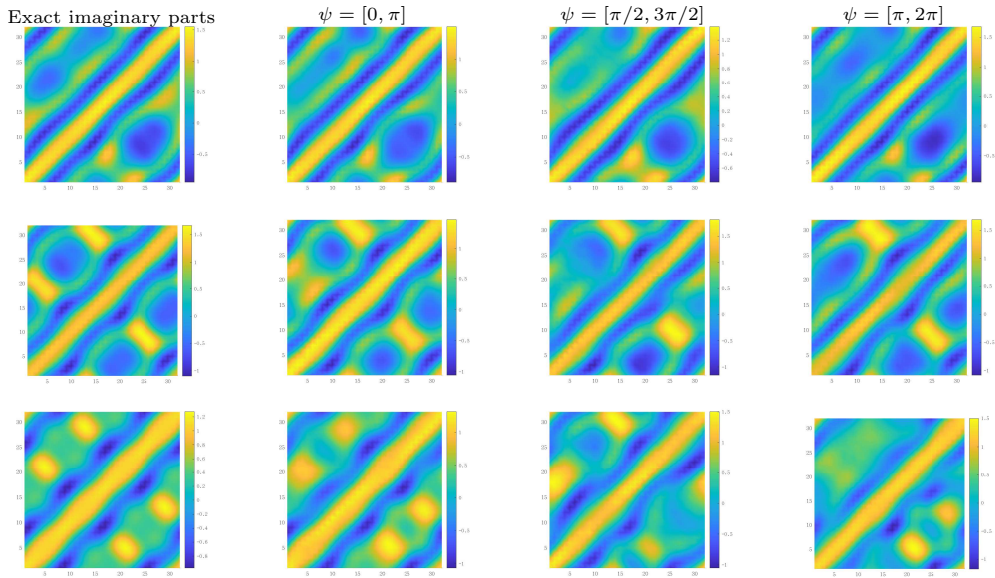


FIG. 4.14. The imaginary parts of obstacles using various incident apertures. Case 1: best-case scenario (Top), Case 2: a pear-shaped obstacle (middle) and Case 3: a rounded square-shaped obstacle (bottom).

- [45] J. Yu, L. Lu, X. Meng, and G. E. Karniadakis. Gradient-enhanced physics-informed neural networks for forward and inverse pde problems. *Computer Methods in Applied Mechanics and Engineering*, 393:114823, 2022.
- [46] Y. Zang, G. Bao, X. Ye, and H. Zhou. Weak adversarial networks for high-dimensional partial differential equations. *Journal of Computational Physics*, 411:109409, 2020.
- [47] D. Zhang, L. Lu, L. Guo, and G. E. Karniadakis. Quantifying total uncertainty in physics-informed neural networks for solving forward and inverse stochastic problems. *Journal of Computational Physics*, 397:108850, 2019.
- [48] M. Zhou, J. Han, M. Rachh, and C. Borges. A neural network warm-start approach for the inverse acoustic obstacle scattering problem. *Journal of Computational Physics*, 490:112341, 2023.

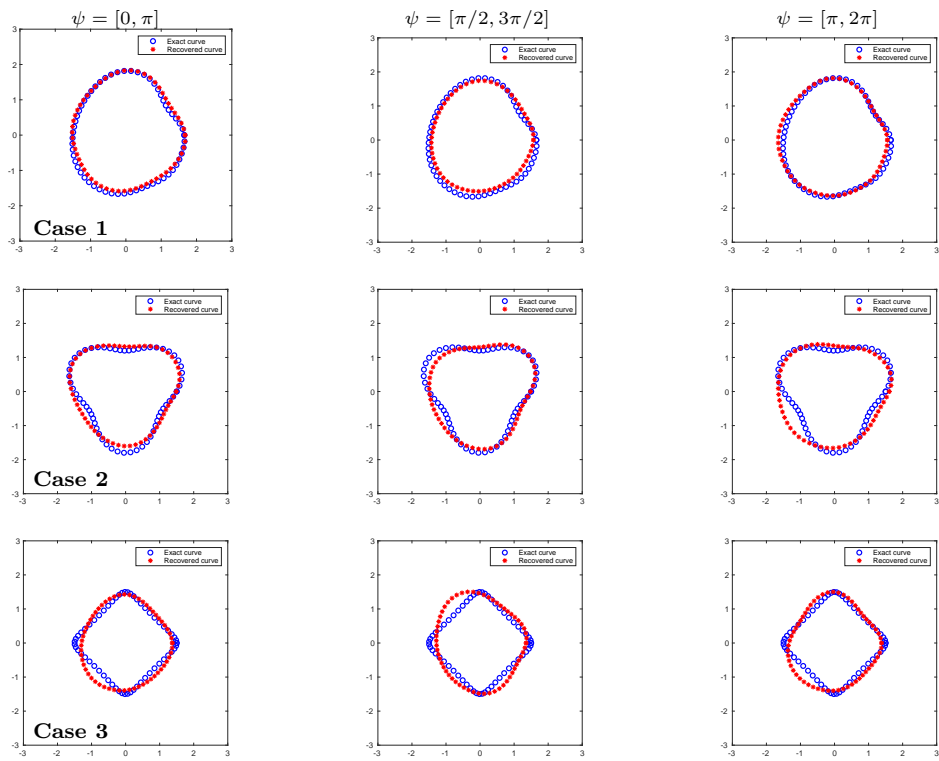


FIG. 4.15. Reconstructions made by DDM using various incident apertures: best-case scenario (Top), a pear-shaped obstacle (middle) and a rounded square-shaped obstacle (bottom).



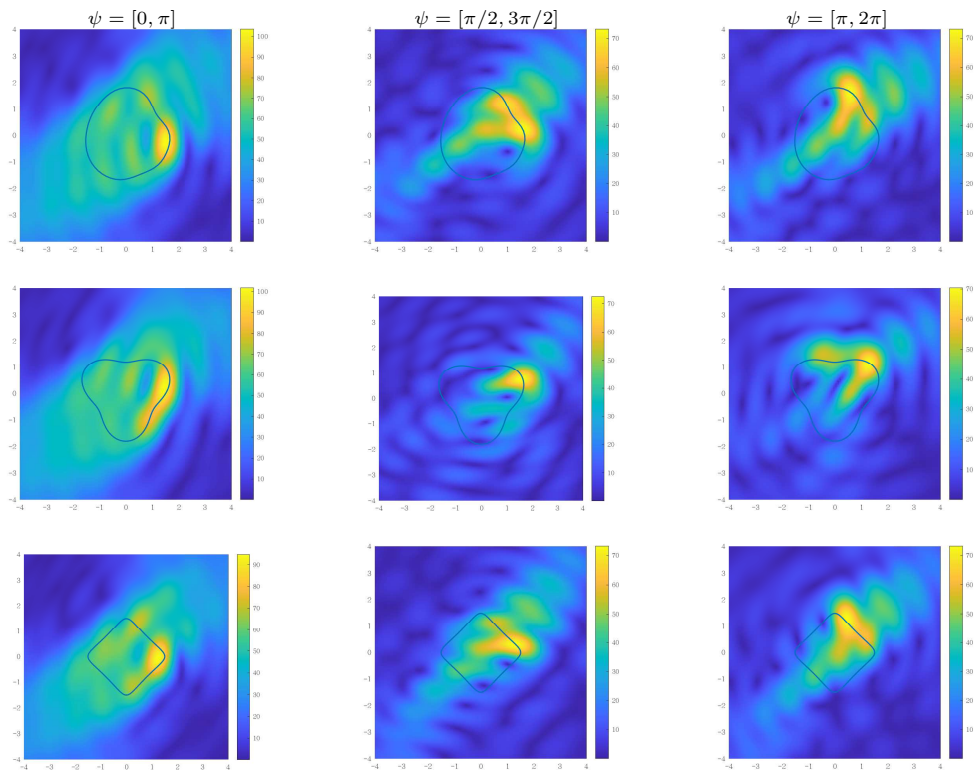


FIG. 4.16. Reconstructions made by DSM using various incident apertures: best-case scenario (Top), a pear-shaped obstacle (middle) and a rounded square-shaped obstacle (bottom).